The Astrophysical Journal, 891:132 (17pp), 2020 March 10 https://doi.org/10.3847/1538-4357/ab76ca
© 2020. The American Astronomical Society. All rights reserved.

How Efficient Is the Streaming Instability in Viscous Protoplanetary Disks?

Kan Chen[1,2] and Min-Kai Lin[2]
[1] Institute of Astronomy, University of Cambridge, Madingley Road, Cambridge CB3 0HA, UK; kc571@cam.ac.uk
[2] Institute of Astronomy and Astrophysics, Academia Sinica, Taipei 10617, Taiwan; mklin@asiaa.sinica.edu.tw
Received 2019 December 27; revised 2020 February 5; accepted 2020 February 14; published 2020 March 13

Abstract

The streaming instability is a popular candidate for planetesimal formation by concentrating dust particles to trigger gravitational collapse. However, its robustness against the physical conditions expected in protoplanetary disks is unclear. In particular, particle stirring by turbulence may impede the instability. To quantify this effect, we develop the linear theory of the streaming instability with external turbulence modeled by gas viscosity and particle diffusion. We find the streaming instability is sensitive to turbulence, with growth rates becoming negligible for alpha viscosity parameters $\alpha \gtrsim \mathrm{St}^{1.5}$, where St is the particle Stokes number. We explore the effect of nonlinear drag laws, which may be applicable to porous dust particles, and find growth rates are modestly reduced. We also find that gas compressibility increases growth rates by reducing the effect of diffusion. We then apply the linear theory to global models of viscous protoplanetary disks. For minimum-mass solar nebula disk models, we find the streaming instability only grows within disk lifetimes beyond tens of astronomical units, even for centimeter-sized particles and weak turbulence ($\alpha \sim 10^{-4}$). Our results suggest it is rather difficult to trigger the streaming instability in nonlaminar protoplanetary disks, especially for small particles.

Unified Astronomy Thesaurus concepts: Planetesimals (1258); Exoplanet formation (492); Hydrodynamics (1963); Planet formation (1241)

1. Introduction

The size and diversity of the exoplanet population suggest that planet formation is an efficient process. Yet, the formation of planetesimals—the building blocks of planets—faces several challenges (Johansen et al. 2014). Dust in protoplanetary disks (PPDs) begins as micron-sized particles, which can grow to millimeter to centimeter sizes via sticking, but growth beyond this size is impeded by bouncing or fragmentation (Blum 2018). Dust may also be lost due to radial drift as a result of gas drag (Whipple 1972).

It is thought that the collective self-gravity of a particle swarm may bypass these barriers by direct gravitational collapse into planetesimals. However, particles must first reach high volume densities relative to the gas for direct collapse (Shi & Chiang 2013). This condition may be attained through dust settling, radial drift, particle traps, or other dust–gas instabilities (Chiang & Youdin 2010; Johansen et al. 2014), such as the "streaming instability" (SI; Youdin & Goodman 2005, hereafter YG05).

The SI is a generic phenomenon in rotating disks of dust and gas that can lead to dust clumping (Johansen & Youdin 2007; Youdin & Johansen 2007; Bai & Stone 2010a, 2010b; Kowalik et al. 2013; Yang & Johansen 2014). Although its physical interpretation is subtle (Jacquet et al. 2011; Lin & Youdin 2017; Squire & Hopkins 2018), direct numerical simulations show that the SI is effective in triggering the direct gravitational collapse of dust clumps (Johansen et al. 2009; Carrera et al. 2015; Simon et al. 2016, 2017; Schäfer et al. 2017; Nesvorný et al. 2019), provided that dust particles have reached sufficient size and the local dust-to-gas mass density ratio is of order unity or larger.

Consequently, the SI is now the de facto mechanism for planetesimal formation and is frequently applied to assess planet formation in complex disk models (Drążkowska & Dullemond 2014; Armitage et al. 2016; Drążkowska et al. 2016; Carrera et al. 2017; Ercolano et al. 2017). However, the numerical experiments that yield the criteria for the SI are often idealized, which may not fully account for the physical conditions expected in real PPDs. Important effects are gas turbulence and particle diffusion (Youdin & Johansen 2007).

PPDs can host a wide range of hydrodynamic and magnetohydrodynamic (MHD) instabilities that drive turbulence. The magnetorotational instability is a powerful mechanism for generating turbulence (Balbus & Hawley 1991), although in PPDs nonideal MHD effects weaken it (e.g., Lesur et al. 2014; Bai 2015; Simon et al. 2018). This gives room for hydrodynamic instabilities to develop, which include the "zombie vortex instability" (Marcus et al. 2015), "convective overstability" (Klahr & Hubbard 2014), and "vertical shear instability" (Nelson et al. 2013). For a recent review of these hydrodynamic instabilities, see Fromang & Lesur (2019), Klahr et al. (2018), Lyra & Umurhan (2019), and references therein.

The effect of the resulting turbulence on the SI has not been explored fully. Selected shearing box simulations have included the magnetorotational instability (e.g., Balsara et al. 2009; Johansen et al. 2011; Yang et al. 2018) or driven turbulence (Gole et al. 2020). However, these computationally intensive calculations prohibit a parameter study to evaluate the efficiency of the SI in global PPDs. A first step toward this goal is to apply linear theory to PPD models. This requires modeling the linear SI in turbulent disks. Some effort in this direction has been taken by Auffinger & Laibe (2018), who included a viscous stress tensor to mimic the effects of gas turbulence.

More recently, Umurhan et al. (2019) extended the original analysis of the SI from YG05 to include both gas viscosity and a corresponding particle diffusion. They find the SI is then limited to a small range of particle sizes at the turbulence strengths expected in PPDs.

Our ultimate goal in this work is to obtain growth timescales and characteristic length scales of the SI in realistic PPDs. This will help us understand the relevance of the SI as a function of

radius in PPDs. We take this opportunity to expand upon Umurhan et al. (2019) by considering compressible gas and exploring nonlinear drag laws. We also present complementary calculations using a simplified "one-fluid" model of dusty gas based on Lin & Youdin (2017) to verify some results.

This paper is organized as follows. In Section 2 we describe the basic, two-fluid framework for studying the linear SI in turbulent disks, including models for gas viscosity and particle diffusion. We list the linearized equations in Section 3 and first present results from controlled numerical experiments in Section 4. In Section 5 we apply linear theory to assess the efficiency of the SI in physical PPD models; finding the SI is limited to large radii at tens of astronomical units. We summarize our results in Section 6, including model caveats and future directions. In the Appendix we present a simplified, one-fluid model of dusty gas to explain some of the results found in the full two-fluid treatment.

2. Basic Equations and Parameters

We consider a protoplanetary disk composed of gas and dust in orbit about a central star of mass M_*. We use $(\rho_g, P, \boldsymbol{V})$ to denote the density, pressure, and velocity of the gas.

We consider a single species of dust treated as a pressureless fluid with density and velocity $(\rho_d, \boldsymbol{W})$ (Jacquet et al. 2011). The two fluids interact via drag parameterized by a single stopping time τ_s, which is prescribed below. A single-species approximation simplifies the analysis considerably. However, it should be noted that this likely overestimates the efficiency of the SI, as suggested by recent generalizations of the SI to multispecies dust in inviscid disks (Krapp et al. 2019).

We neglect disk self-gravity and magnetic fields. For simplicity, we also neglect the vertical component of stellar gravity and consider unstratified disks. However, in numerical calculations we will account for stratification when choosing physical parameter values.

In an inertial frame with cylindrical coordinates (R, ϕ, z) centered on the star, this two-fluid disk is governed by the following equations:

$$\frac{\partial \rho_g}{\partial t} + \nabla \cdot (\rho_g \boldsymbol{V}) = 0, \tag{1}$$

$$\frac{\partial \rho_d}{\partial t} + \nabla \cdot (\rho_d \boldsymbol{W}) = \nabla \cdot \left[D \rho_g \nabla \left(\frac{\rho_d}{\rho_g} \right) \right], \tag{2}$$

$$\frac{\partial \boldsymbol{V}}{\partial t} + \boldsymbol{V} \cdot \nabla \boldsymbol{V} = -\frac{1}{\rho_g} \nabla P - \Omega_K^2 R \hat{\boldsymbol{R}} + \frac{1}{\rho_g} \nabla \cdot \boldsymbol{T} + \frac{\epsilon}{\tau_s} (\boldsymbol{W} - \boldsymbol{V}), \tag{3}$$

$$\frac{\partial \boldsymbol{W}}{\partial t} + \boldsymbol{W} \cdot \nabla \boldsymbol{W} = -\Omega_K^2 R \hat{\boldsymbol{R}} - \frac{1}{\tau_s} (\boldsymbol{W} - \boldsymbol{V}), \tag{4}$$

where D is a constant diffusion coefficient (Morfill & Voelk 1984), $\Omega_K(R) = \sqrt{GM_*/R^3}$ is the Keplerian frequency, G is the gravitational constant, $\epsilon = \rho_d/\rho_g$ is the local dust-to-gas ratio, and τ_s is the particle stopping time. We consider isothermal gas so that $P = c_s^2 \rho_g$, where $c_s = H_g \Omega_K$ is a prescribed sound speed and H_g is a nominal gas disk thickness.

We assume dust particles are subject to diffusion due to turbulent stirring from the gas. In Equation (3) we thus include a viscous stress tensor $\boldsymbol{T}$ to model gas turbulence:

$$\boldsymbol{T} = \rho_g \nu \left[\nabla \boldsymbol{V} + (\nabla \boldsymbol{V})^\dagger - \frac{2}{3} \boldsymbol{I} \nabla \cdot \boldsymbol{V} \right], \tag{5}$$

where ν is the kinematic viscosity and $\boldsymbol{I}$ is the identity tensor. The last term in the momentum equations models dust–gas drag and is described below.

2.1. Local Description

We consider the local stability of the dusty disk. To do so, we focus on a small patch of the disk and adopt the shearing box framework (Goldreich & Lynden-Bell 1965). The shearing box is centered at a point $(R_0, \phi_0, 0)$ that rotates about the star with angular frequency $\Omega_K(R_0) \equiv \Omega_0$, so $\phi_0 = \Omega_0 t$. Cartesian coordinates (x, y, z) in the shearing box correspond to the (R, ϕ, z) directions in the global disk. Global curvature terms are neglected, as are radial gradients in densities and disk temperature.

In this frame, Keplerian rotation appears as a linear shear flow, $-q\Omega_0 x \hat{\boldsymbol{y}}$ with $q = 3/2$. We also define $\boldsymbol{w}, \boldsymbol{v}$ as the velocity deviations from the background Keplerian shear in the rotating, local frame. That is,

$$\boldsymbol{w} = \boldsymbol{W} - (R - qx)\Omega_0 \hat{\boldsymbol{y}}, \tag{6}$$

and similarly for $\boldsymbol{v}$. For clarity we drop the subscript "0" below.

In terms of velocity fluctuations, the two-fluid shearing box equations read as

$$\frac{\partial \rho_d}{\partial t} + \nabla \cdot (\rho_d \boldsymbol{w}) - q\Omega x \frac{\partial \rho_d}{\partial y} = \nabla \cdot \left[D \rho_g \nabla \left(\frac{\rho_d}{\rho_g} \right) \right], \tag{7}$$

$$\frac{\partial \rho_g}{\partial t} + \nabla \cdot (\rho_g \boldsymbol{v}) - q\Omega x \frac{\partial \rho_g}{\partial y} = 0, \tag{8}$$

$$\frac{\partial \boldsymbol{w}}{\partial t} + \boldsymbol{w} \cdot \nabla \boldsymbol{w} - q\Omega x \frac{\partial \boldsymbol{w}}{\partial y} = 2\Omega w_y \hat{\boldsymbol{x}} - \frac{\kappa^2}{2\Omega} w_x \hat{\boldsymbol{y}} - \frac{1}{\tau_s} (\boldsymbol{w} - \boldsymbol{v}), \tag{9}$$

$$\frac{\partial \boldsymbol{v}}{\partial t} + \boldsymbol{v} \cdot \nabla \boldsymbol{v} - q\Omega x \frac{\partial \boldsymbol{v}}{\partial y} = 2\Omega v_y \hat{\boldsymbol{x}} - \frac{\kappa^2}{2\Omega} v_x \hat{\boldsymbol{y}} - c_s^2 \nabla \ln \rho_g + 2\eta \Omega^2 R \hat{\boldsymbol{x}} + \frac{1}{\rho_g} \nabla \cdot \boldsymbol{T} + \frac{\epsilon}{\tau_s} (\boldsymbol{w} - \boldsymbol{v}). \tag{10}$$

The SI only operates in the presence of a global pressure gradient. To include this effect in a local model, we add a constant forcing in the gas momentum Equation (10), $2\eta\Omega^2 R \hat{\boldsymbol{x}}$, where

$$\eta \equiv -\frac{1}{2R\Omega^2} \frac{1}{\rho_g} \frac{\partial P}{\partial R} \tag{11}$$

is a dimensionless measure of the global pressure gradient (Youdin & Goodman 2005). This term causes a relative drift between dust and gas (see Section 2.5) and is essential for the streaming instability.

The basic Equations (2)–(10) are the same as that in Youdin & Johansen (2007) with the addition of gas viscosity and particle diffusion.

2.2. Generalized Stopping Times

The magnitude of dust–gas drag is described by the stopping time τ_s, which is the characteristic decay timescale for a dust particle's velocity relative to the gas, $\Delta v \equiv |\boldsymbol{v} - \boldsymbol{w}|$. A smaller τ_s indicates stronger coupling between gas and dust.

Physically, τ_s depends on the particle size a_p, its internal density $\rho_\bullet$, its relative drift Δv, the gas density, and the sound speed (Whipple 1972; Weidenschilling 1977). The specific form of $\tau_s(a_p, \rho_\bullet, \Delta v, \rho_g, c_s)$ depends on the particle size relative to the mean free path of gas molecules, $\lambda_{\rm mfp}$. Particles with $a_p \lesssim 9\lambda_{\rm mfp}/4$ are in the Epstein regime with

$$\tau_s^{\rm Epstein} = \frac{a_p \rho_\bullet}{c_s \rho_g}. \tag{12}$$

We remark that most studies of the SI assume an Epstein drag law.

Particles with $a_p \gtrsim 9\lambda_{\rm mfp}/4$ enter the Stokes regime. In this case, τ_s also depends on the Reynolds number defined by ${\rm Re} \equiv 2a\Delta v/\nu_m$, where $\nu_m \equiv (1/2) c_s \lambda_{\rm mfp}$ is the gas molecular viscosity:

$$\tau_s^{\rm Stokes} = \begin{cases} \dfrac{2\rho_\bullet a_p^2}{9\nu_m \rho_g} & {\rm Re} < 1, \\ \dfrac{2^{0.6}\rho_\bullet a_p^{1.6}}{9\nu_m^{0.6}\rho_g^{1.4}\Delta v^{0.4}} & 1 < {\rm Re} < 800, \\ \dfrac{6\rho_\bullet a_p}{\rho_g \Delta v} & {\rm Re} > 800 \end{cases} \tag{13}$$

(Birnstiel et al. 2010). Note that $\lambda_{\rm mfp} \propto 1/\rho_g$.

One goal of this work is to examine the effect of nonlinear drag laws, that is, when τ_s itself depends on the relative drift. As such, instead of adopting different functional forms of τ_s that depend on the physical conditions, we use the following generalized form of τ_s:

$$\tau_s = \tau_{s,\rm eqm} \frac{\rho_{g,\rm eqm}^a |\boldsymbol{w} - \boldsymbol{v}|_{\rm eqm}^b}{\rho_g^a |\boldsymbol{w} - \boldsymbol{v}|^b}, \tag{14}$$

where a, b are constant parameters, and subscript "eqm" denotes equilibrium values.

Equation (14) encapsulates the different drag laws described in Equations (12)–(13). For example, the Epstein regime corresponds to $a = 1$, $b = 0$, and the fully nonlinear Stokes law for ${\rm Re} > 800$ corresponds to $a = b = 1$. We find results are insensitive to the index a because the SI does not require compressible gas (Youdin & Goodman 2005). We thus fix $a = 1$ for all calculations presented below.

For convenience, we also define the Stokes number St as a dimensionless measure of the (equilibrium) stopping time:

$${\rm St} \equiv \tau_{s,\rm eqm}\Omega. \tag{15}$$

For the most commonly considered case of Epstein drag, St is equivalent to the particle size for fixed internal densities, because c_s is constant and the SI depends weakly on ρ_g.

2.3. Gas Turbulence

We adapt the standard alpha prescription for modeling gas turbulence (Shakura & Sunyaev 1973):

$$\nu = \alpha c_s H_g \left(\frac{\rho_g}{\rho_{g,\rm eqm}}\right)^\xi, \tag{16}$$

where α is the dimensionless viscosity and ξ is a free parameter. In practice, we take $\xi = -1$ so that the dynamic viscosity $\rho_g \nu$ is constant to avoid viscous overstabilities (Latter & Ogilvie 2006).

2.4. Dust Diffusion

We parameterize particle diffusion via the dimensionless coefficient δ such that

$$D = \delta c_s H_g, \tag{17}$$

and δ is related to the gas viscosity by

$$\delta = \frac{1 + {\rm St} + 4{\rm St}^2}{(1 + {\rm St}^2)^2}\alpha \tag{18}$$

(Youdin & Lithwick 2007; Youdin 2011). For small particles with ${\rm St} \ll 1$, we have $\delta \simeq \alpha$.

2.5. Two-fluid Equilibrium

The two-fluid shearing box Equations (7)–(10) admit an axisymmetric, steady state with constant ρ_d and ρ_g and no vertical velocities, $w_z = v_z = 0$. The horizontal velocity fluctuations relative to the Keplerian flow are

$$w_x = -\frac{2{\rm St}}{\Delta^2}\eta R\Omega_K, \tag{19}$$

$$w_y = -\frac{1 + \epsilon}{\Delta^2}\eta R\Omega_K, \tag{20}$$

$$v_x = \frac{2\epsilon\,{\rm St}}{\Delta^2}\eta R\Omega_K, \tag{21}$$

$$v_y = -\frac{1 + \epsilon + {\rm St}^2}{\Delta^2}\eta R\Omega_K, \tag{22}$$

where

$$\Delta^2 = {\rm St}^2 + (1 + \epsilon)^2. \tag{23}$$

For typical disk models with $\eta > 0$ (a negative pressure gradient), particles drift inward while gas is pushed out by the mutual drag force.

2.6. Connection with Stratified Disks

In an unstratified disk model, the equilibrium dust-to-gas ratio ϵ and dust diffusion coefficient D, which is determined by the gas viscosity (Equations (17)–(18)), can be set independently. Indeed, we take this approach in our initial calculations.

Physically, however, an unstratified model represents the disk midplane, and vertical dust settling is balanced by turbulent diffusion (e.g., Fromang & Papaloizou 2006; Stoll & Kley 2016; Flock et al. 2017; Yang et al. 2018; Lin 2019). In this case, ϵ and D are no longer independent. The characteristic

dust layer thickness $H_{\rm d}$ can be modeled by

$$H_{\rm d} = \sqrt{\frac{\delta}{{\rm St}+\delta}} H_{\rm g}, \tag{24}$$

(Dubrulle et al. 1995; Lin 2019). The midplane dust-to-gas ratio ϵ is given by

$$\epsilon = Z\frac{H_{\rm g}}{H_{\rm d}} \tag{25}$$

(Johansen et al. 2014), where the local metallicity Z is

$$Z = \frac{\Sigma_{\rm d}}{\Sigma_{\rm g}}, \tag{26}$$

where $\Sigma_{\rm d,g}$ are the surface densities in dust and gas, respectively. In our self-consistent calculations, we determine ϵ by specifying the metallicity Z, Stokes number St, and gas viscosity α (and hence δ).

2.7. One-fluid Models

In addition to the full, two-fluid treatment of dusty gas described above, we also supplement some of our calculations with the "one-fluid" model of dusty gas first described by Laibe & Price (2014) and Price & Laibe (2015) and further developed by Lin & Youdin (2017). In the Appendix we extend the one-fluid model to include dust diffusion and nonlinear drag laws and compare it with the full two-fluid treatment.

3. Linear Problem

3.1. Perturbation Equations

We perturb the above two-fluid system with axisymmetric Eulerian perturbations such that

$$\rho_{\rm g} \rightarrow \rho_{\rm g} + \delta\rho_{\rm g} \exp\left[{\rm i}(k_x x + k_z z) + \sigma t\right] \tag{27}$$

and similarly for other variables, where $k_{x,z}$ are radial and vertical wavenumbers and taken to be positive without loss of generality; σ is the complex frequency with growth rate $s \equiv {\rm Re}(\sigma)$.

After we drop the "eqm" subscripts for clarity, the linearized equations for the dust fluid read as

$$\sigma\frac{\delta\rho_{\rm d}}{\rho_{\rm d}} = -{\rm i}k_x w_x \frac{\delta\rho_{\rm d}}{\rho_{\rm d}} - {\rm i}k_x\delta w_x - {\rm i}k_z\delta w_z - Dk^2\left(\frac{\delta\rho_{\rm d}}{\rho_{\rm d}} - \frac{\delta\rho_{\rm g}}{\rho_{\rm g}}\right), \tag{28}$$

$$\sigma\delta w_x = -{\rm i}k_x w_x\delta w_x + 2\Omega\delta w_y + \frac{1}{\tau_{\rm s}}(w_x - v_x)\left(\frac{\delta\tau_{\rm s}}{\tau_{\rm s}}\right) - \frac{1}{\tau_{\rm s}}(\delta w_x - \delta v_x), \tag{29}$$

$$\sigma\delta w_y = -{\rm i}k_x w_x\delta w_y - \frac{\Omega}{2}\delta w_x + \frac{1}{\tau_{\rm s}}(w_y - v_y)\left(\frac{\delta\tau_{\rm s}}{\tau_{\rm s}}\right) - \frac{1}{\tau_{\rm s}}(\delta w_y - \delta v_y), \tag{30}$$

$$\sigma\delta w_z = -{\rm i}k_x w_x\delta w_z - \frac{1}{\tau_{\rm s}}(\delta w_z - \delta v_z), \tag{31}$$

and that for the gas equations are

$$\sigma\frac{\delta\rho_{\rm g}}{\rho_{\rm g}} = -{\rm i}k_x v_x\frac{\delta\rho_{\rm g}}{\rho_{\rm g}} - {\rm i}k_x\delta v_x - {\rm i}k_z\delta v_z, \tag{32}$$

$$\sigma\delta v_x = -{\rm i}k_x v_x\delta v_x + 2\Omega\delta v_y - {\rm i}k_x c_s^2\frac{\delta\rho_{\rm g}}{\rho_{\rm g}} + \delta F_x^{\rm visc} - \frac{\epsilon}{\tau_{\rm s}}(w_x - v_x)\left[\frac{\delta(\tau_{\rm s}\rho_{\rm g})}{\tau_{\rm s}\rho_{\rm g}} - \frac{\delta\rho_{\rm d}}{\rho_{\rm d}}\right] + \frac{\epsilon}{\tau_{\rm s}}(\delta w_x - \delta v_x), \tag{33}$$

$$\sigma\delta v_y = -{\rm i}k_x v_x\delta v_y - \frac{\Omega}{2}\delta v_x + \delta F_y^{\rm visc} - \frac{\epsilon}{\tau_{\rm s}}(w_y - v_y)\left[\frac{\delta(\tau_{\rm s}\rho_{\rm g})}{\tau_{\rm s}\rho_{\rm g}} - \frac{\delta\rho_{\rm d}}{\rho_{\rm d}}\right] + \frac{\epsilon}{\tau_{\rm s}}(\delta w_y - \delta v_y), \tag{34}$$

$$\sigma\delta v_z = -{\rm i}k_x v_x\delta v_z - {\rm i}k_z c_s^2\frac{\delta\rho_{\rm g}}{\rho_{\rm g}} + \delta F_z^{\rm visc} + \frac{\epsilon}{\tau_{\rm s}}(\delta w_z - \delta v_z). \tag{35}$$

In the above equations, the linearized viscous forces are

$$\delta F_x^{\rm visc} = -\nu\left(k_z^2 + \frac{4}{3}k_x^2\right)\delta v_x - \frac{1}{3}\nu k_x k_z\delta v_z, \tag{36}$$

$$\delta F_y^{\rm visc} = -\nu(k_z^2 + k_x^2)\delta v_y, \tag{37}$$

$$\delta F_z^{\rm visc} = -\nu\left(\frac{4}{3}k_z^2 + k_x^2\right)\delta v_z - \frac{1}{3}\nu k_x k_z\delta v_x \tag{38}$$

(Lin & Kratter 2016), and the linearized stopping time is

$$\frac{\delta\tau_{\rm s}}{\tau_{\rm s}} = -a\frac{\delta\rho_{\rm g}}{\rho_{\rm g}} - \frac{b}{|\boldsymbol{w}-\boldsymbol{v}|^2}[(w_x - v_x)(\delta w_x - \delta v_x) + (w_y - v_y)(\delta w_y - \delta v_y)]. \tag{39}$$

Equations (28)–(35) constitute an eigenvalue problem

$$\boldsymbol{M}\boldsymbol{q} = \sigma\boldsymbol{q}, \tag{40}$$

where $\boldsymbol{q} = (\delta\rho_{\rm d}, \delta\boldsymbol{w}, \delta\rho_{\rm d}, \delta\boldsymbol{v})^{\rm T}$ is the eigenvector and $\boldsymbol{M}$ is the matrix representation of the right-hand side of Equations (28)–(35). We solve this eigenvalue problem with standard matrix routines provided by the LAPACK package.[3]

3.2. Dimensionless Parameters

We solve the stability problem numerically to find the dimensionless SI growth rate $S \equiv s/\Omega$ as a function of the following parameters:

1. St: the Stokes number or particle size.
2. $\epsilon = \rho_{\rm d}/\rho_{\rm g}$: the equilibrium dust-to-gas ratio. This is either set directly or indirectly via the total metallicity Z (see Section 2.6).
3. α: the gas viscosity parameter, which also determines the particle diffusion strength δ.

[3] http://www.netlib.org/lapack/

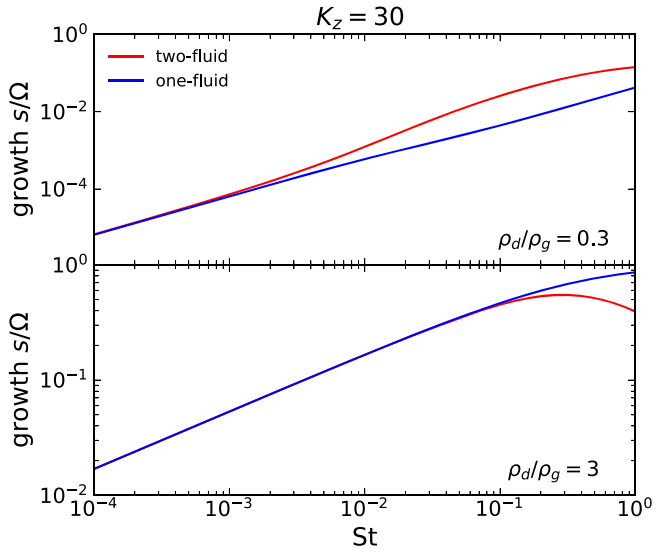

Figure 1. Normalized streaming instability growth rates as a function of Stokes number St in the full two-fluid (red) and simplified one-fluid (blue) models using the Epstein drag law ($\tau_s \propto 1/\rho_g$) without viscosity or diffusion ($\nu = D = 0$) The dust-to-gas ratio is $\epsilon = 0.3$ (upper) and $\epsilon = 3$ (lower). We fix $K_z = 30$ and plot the maximum growth rate over K_x. The one-fluid results are obtained from solving Equations (67)–(71).

4. b: the power-law index that determines the degree of nonlinearity in the drag law.
5. $K_{x,z} \equiv k_{x,z}\eta R$: the dimensionless perturbation wavenumbers.

We also normalize velocities by $\eta R\Omega$. Together with the above normalizations, the linearized equations may be rendered dimensionless, in which case η appears as $\eta R\Omega/c_s \equiv \hat{\eta}$ and becomes a measure for gas compressibility (Youdin & Johansen 2007). We set $\hat{\eta} = 0.05$ unless otherwise stated.

4. Results

4.1. Epstein Drag in Inviscid Disks

We begin with a fiducial setup assuming Epstein drag $(a, b) = (1, 0)$ without viscosity or diffusion ($\alpha = \delta = 0$). This is the standard case considered in previous analytic SI calculations (Youdin & Goodman 2005; Kowalik et al. 2013). Following Youdin & Goodman, we fix K_z (=30 here) and maximize growth rates over K_x. We find qualitatively similar behavior for other fixed values of K_z. For the cases examined below, we find the optimum K_x decreases from $O(10^{2-3})$ at $\mathrm{St} = 10^{-4}$ to $O(10^{0-1})$ at $\mathrm{St} = 1$.

In Figure 1 we plot growth rates as a function of St for two dust-to-gas ratios: a dust-poor disk with $\epsilon = 0.3$ and a dust-rich disk with $\epsilon = 3$. We limit the Stokes number $\mathrm{St} < 1$ because larger particles violate the fluid approximation (Jacquet et al. 2011). To check our results, we also plot corresponding growth rates obtained from the one-fluid framework described in the Appendix. Our two-fluid results are consistent with earlier calculations (Youdin & Goodman 2005; Youdin & Johansen 2007).

We find the one-fluid approximation is accurate for $\mathrm{St} \lesssim 0.1$ when $\epsilon > 1$. However, for $\epsilon < 1$, the one-fluid model only reproduces the full two-fluid results for $\mathrm{St} \lesssim 10^{-3}$. Notice also that the one-fluid model tends to overestimate (underestimate) SI growth rates in dust-rich (dust-poor) disks.

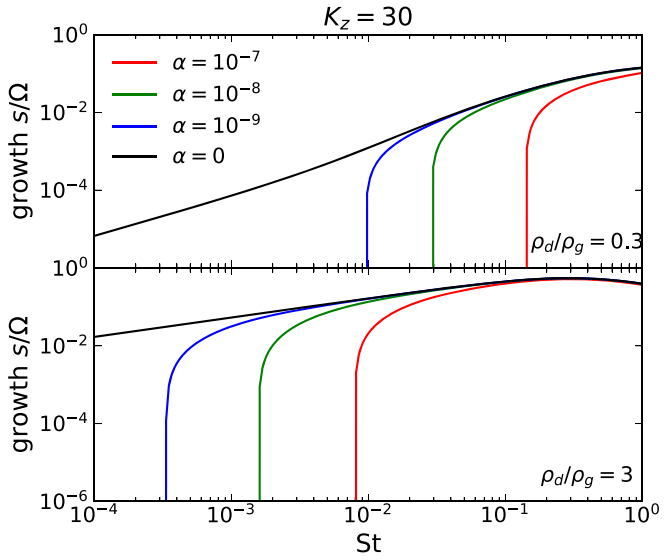

Figure 2. Streaming instability growth rates as a function of St in turbulent disks with particle diffusion. We fix $K_z = 30$ and optimize growth rates over K_x. Colors of lines denote different values of the gas viscosity parameter α.

4.2. Effect of Turbulence

We now examine turbulent disks by including a gas viscosity $\alpha \neq 0$, which determines the particle diffusion coefficient δ from Equation (18). We continue with the Epstein drag law with $a = 1$, $b = 0$. We either set the dust-to-gas ratio directly as a free parameter or physically via the total metallicity $Z = \Sigma_d/\Sigma_g$. We discuss these approaches separately.

All results in this section are obtained from the full two-fluid equations. In Appendix A.4 we develop a simplified analytic model from the one-fluid approximation, which only includes dust diffusion.

4.2.1. Fixed Local Dust-to-gas Ratios

For fixed ρ_d/ρ_g, turbulence only takes effect through the perturbation equations (see fixed metallicity considered later).

Figure 2 shows growth rates as a function of St for $\alpha = 0$, 10^{-9}, 10^{-8}, 10^{-7} for fixed $K_z = 30$ and maximized over K_x. Notice that even such small values of α significantly stabilize the SI. For fixed K_z we find there exists a minimum Stokes number, $\mathrm{St}_{\min}$, for the SI to exist. Note that $\mathrm{St}_{\min}$ generally increases with larger α but decreases with increasing ρ_d/ρ_g. This implies that in turbulent disks, larger particles or higher dust-to-gas ratios are required for the SI. Equivalently said, small particles are more sensitive to turbulence than larger particles. We find the optimum radial wavenumber decreases from $K_x \sim 10^3$ for $\mathrm{St} = 10^{-4}$ to $K_x \sim 1$ for $\mathrm{St} = 1$, but is insensitive to α. As shown below, we speculate this is due to viscosity having a larger impact on the SI's vertical structure (which is fixed here) than the radial wavenumber.

Next, we optimize growth rates over K_z as well. Figure 3 shows the optimum growth rates and wavenumbers for both a dust-poor and dust-rich disk. For a given St, growth rates fall below $10^{-6}\Omega$ when the turbulence exceeds some critical value $\alpha_{\max}$, which increases with St. However, unlike for fixed-K_z calculations, here both dust-rich and dust-poor disks have similar values of $\alpha_{\max}$.

The middle and right panels of Figure 3 show the corresponding optimum wavenumbers. As expected, increasing

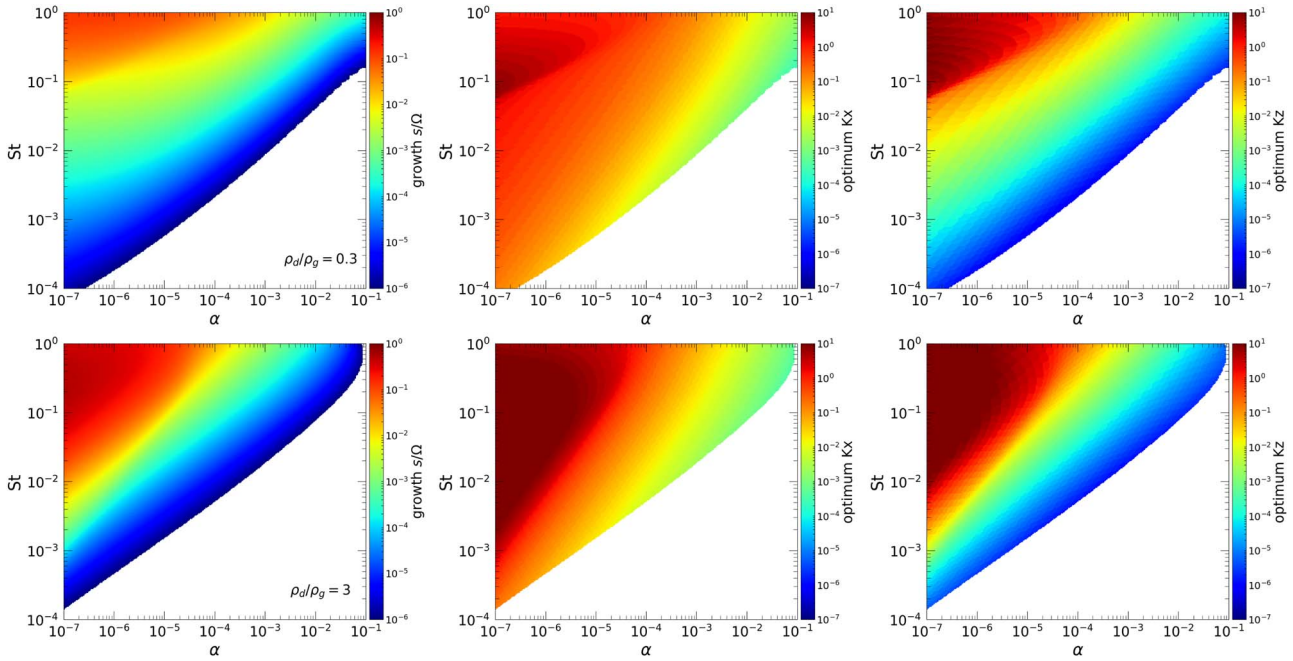

Figure 3. Streaming instability growth rates (left) and optimum radial and vertical wavenumbers (middle, right) as a function of gas viscosity with a corresponding dust diffusion coefficient and Stokes number St for fixed dust-to-gas ratios $\epsilon = 0.3$ (top) and $\epsilon = 3$ (bottom). We truncate the plots for $s < 10^{-6}\Omega$.

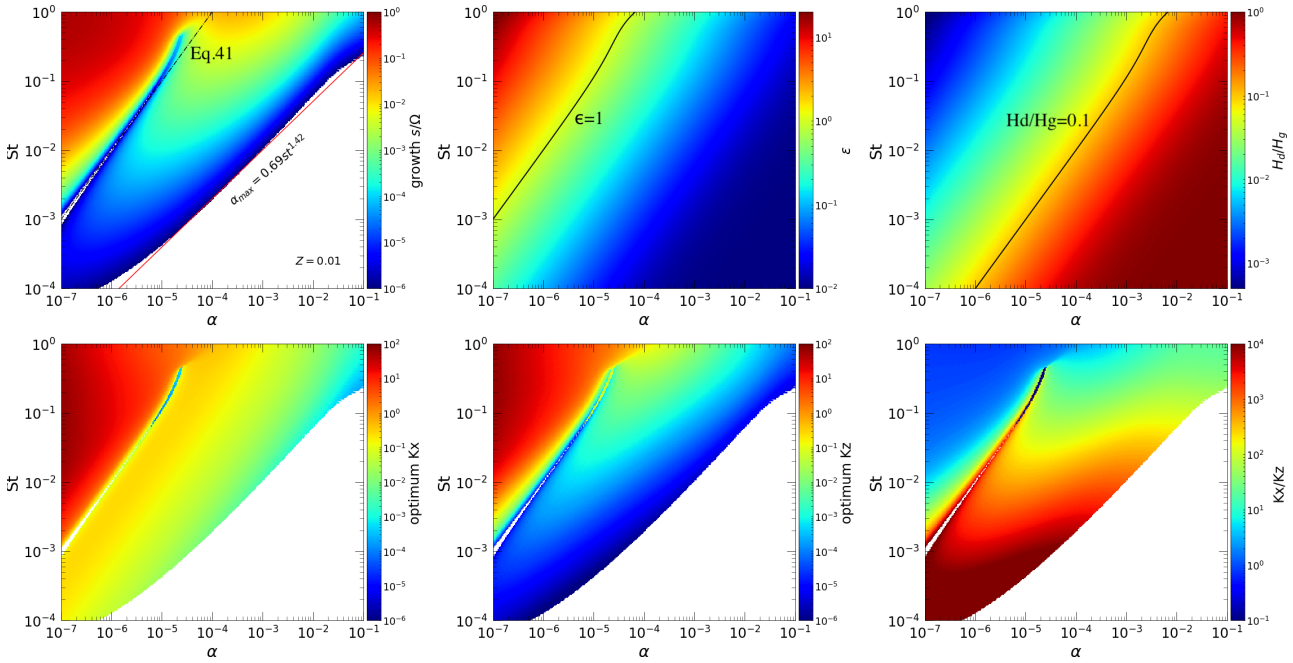

Figure 4. Growth rates (upper left) with fixed metallicity $Z = 0.01$ as a function of Stokes number and gas viscosity (with a corresponding particle diffusion coefficient). The red line is an empirical fit to the maximum allowed α, beyond which growth rates become negligible ($<10^{-6}\Omega$). The black dotted–dashed line corresponds to Equation (41). The dust-to-gas ratio (upper middle) and dust scale height normalized by the gas scale height (upper right) are also shown. We also mark some characteristic contours with black lines in these two panels, namely $\epsilon = 1$ and $H_d/H_g = 0.1$. The corresponding optimum wavenumbers, K_x, K_z, and their ratio K_x/K_z, are shown in the lower left, middle, and right panels, respectively.

the viscosity generally increases the SI length scales. Notice also for fixed St and increasing viscosity that $K_z \ll K_x$, implying that turbulence smears out the SI more easily in the vertical direction.

4.2.2. Fixed Local Metallicities

We now consider a more physical setup by fixing the total metallicity $Z \equiv \Sigma_d/\Sigma_g$ and setting the dust-to-gas ratio $\epsilon \equiv \rho_d/\rho_g$ in accordance with dust settling (Equation (25)). In this case, ρ_d/ρ_g also depends on the Stokes number St and particle diffusion coefficient δ, which itself is determined by the gas viscosity α (Equation (18)). That is, the basic state now also varies with turbulence strength.

As a fiducial case, we set $Z = 0.01$ and plot growth rates and optimum wavenumbers $K_{x,z}$ in Figure 4, along with ϵ and H_d/H_g. The dust-to-gas ratio ranges from $\sim 10^{-2}$ to 20, while

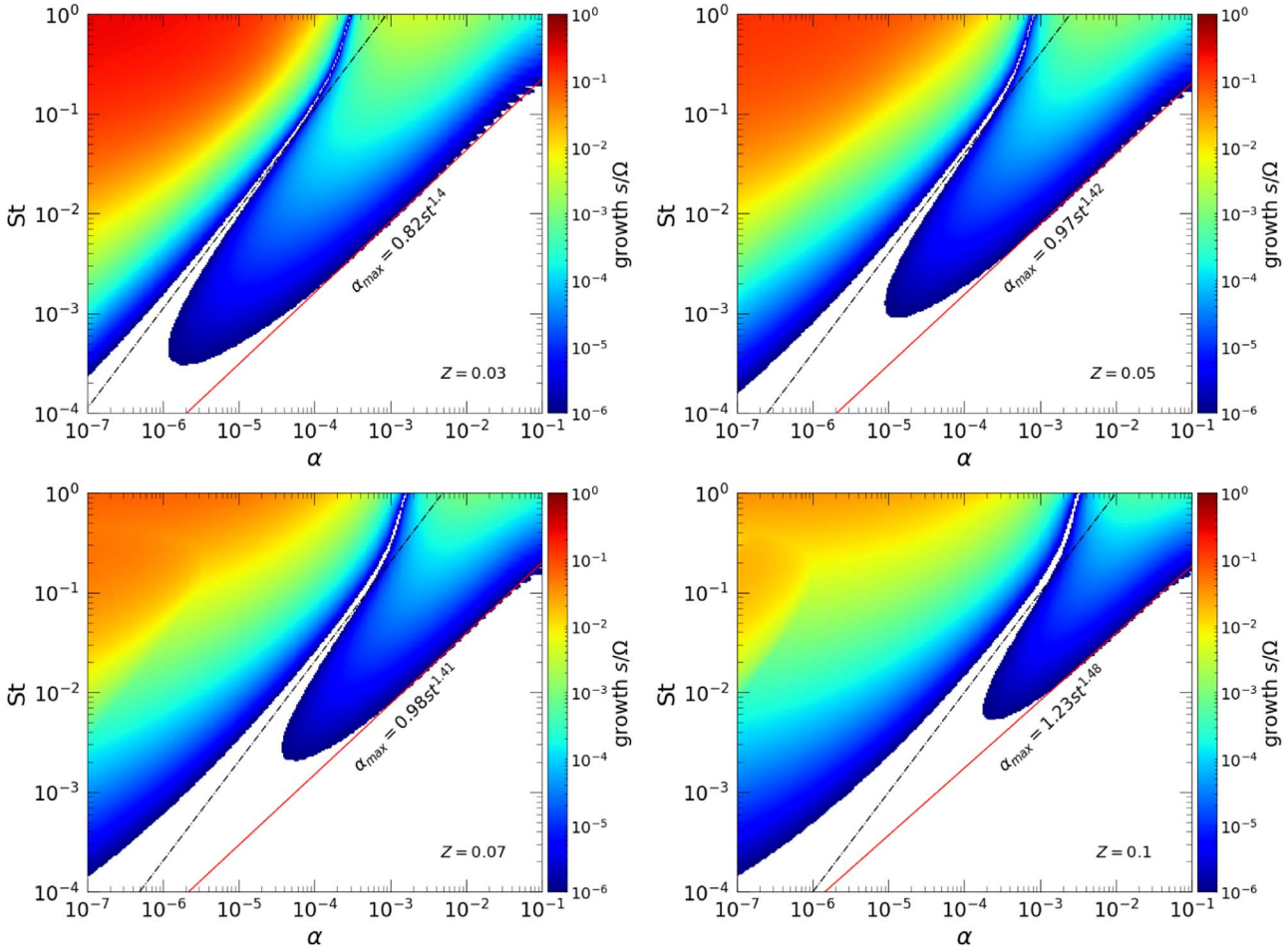

Figure 5. Growth rates as a function of St and α for different metallicities Z. The black dotted–dashed lines correspond to Equation (41), while red lines are empirical fits to the maximum allowed α for growth rates to remain $>10^{-6}\Omega$.

H_d/H_g ranges from 10^{-3} to unity. The gap in the upper left of the figure corresponds to $\epsilon \sim 1$ where the SI is quenched (Youdin & Goodman 2005); see also Appendix A.5.

As before, larger St and smaller α give higher growth rates. The dust-rich SI (left of the gap) involves smaller wavelengths than the dust-poor SI (right of the gap) because viscosity is larger in the latter case. Interestingly, we find $K_x < K_z$ for the dust-rich SI, while $K_x > K_z$ for the dust-poor SI. This implies with high viscosity that the SI becomes vertically unstructured.

SI growth rates are only dynamical ($\sim\Omega$) for $\epsilon > 1$ (Youdin & Goodman 2005). From Equation (25), this requires $Z\sqrt{(\mathrm{St}+\delta)/\delta} > 1$. For small St we can approximate $\delta \simeq \alpha$. Thus the dynamical SI is limited to

$$\alpha \lesssim \frac{Z^2}{1-Z^2}\mathrm{St} \simeq Z^2\mathrm{St}, \tag{41}$$

where the last equality assumes $Z \ll 1$. It should be noted that here SI is quenched because the background dust-to-gas ratio approaches unity as viscosity is increased from zero, as opposed to the perturbations being stabilized by viscosity.

At fixed St, increasing α eventually pushes the system into the dust-poor regime of the SI ($\epsilon < 1$), which is slower than dynamical. Physically this is due to dust becoming vertically mixed by gas turbulence. As viscosity increases further, the SI is reduced to negligible growth rates.

Figure 5 shows the growth rates as a function of St and α for other metallicities $Z = 0.03$, 0.05, 0.07, and 0.1. The red line in each panel is a fit to the maximum α as a function of St. These contour plots are essentially translations of that for $Z = 0.01$ (to the upper right). As expected, increasing dust loading expands the region of the dust-rich SI. Its boundary becomes less well approximated by Equation (41), but it is clear that SI can persist in more turbulent disks if the overall dust content is increased. Notice, however, that the dust-rich SI in fact slows down with increasing Z. This is because the SI is also quenched in the limit of gas-free disks (Youdin & Goodman 2005).

We estimate from Figures 4–5 a maximum viscosity $\alpha_{\max} \sim \mathrm{St}^{1.5}$ above which growth rates become negligible ($<10^{-6}\Omega$). This relation varies weakly with our choice of minimum growth rates or metallicity. Thus, the SI is rapidly quenched by viscosity for small particles.

4.3. Nonlinear Drag Laws

Here we consider the effect of different drag laws on the SI. Recall from Section 2.2 that our stopping times are parameterized as $\tau_s \propto \rho_g^{-a}|\boldsymbol{w}-\boldsymbol{v}|^{-b}$. We find the SI is insensitive to a. Thus, we fix $a = 1$ and focus on the effect of b, that is, the degree of nonlinearity. We consider drag laws with $b = 0.4$ and $b = 1$.

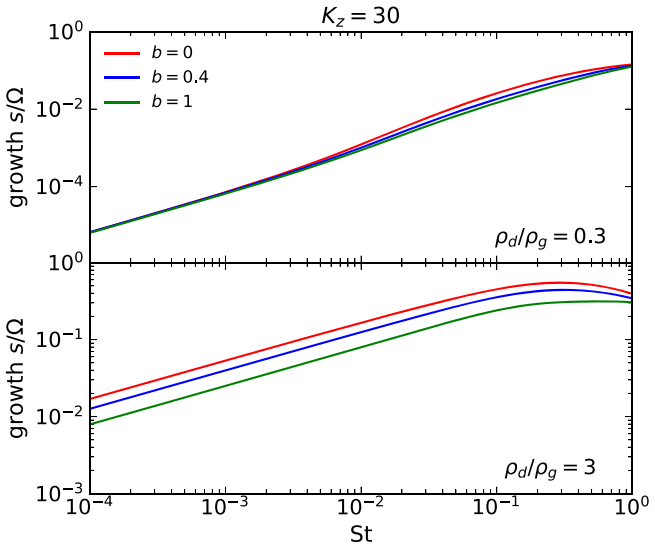

Figure 6. Streaming instability growth rates in inviscid disks as a function of Stokes number for different drag laws with $b = 0$ (red, linear drag), 0.4 (blue, nonlinear drag), and 1 (green, quadratic drag) for $\epsilon = 0.3$ (top) and $\epsilon = 3$ (bottom).

4.3.1. Inviscid Disks

We first return to inviscid disks ($\alpha = \delta = 0$) to isolate the effect of the drag law. Figure 6 shows growth rates as a function of Stokes number with $\epsilon = 0.3$ and $\epsilon = 3$ for $K_z = 30$ and maximized over K_x. We find the optimum K_x does not vary significantly with b.

Increasing the degree of nonlinearity reduces SI growth rates. This effect is small in dust-poor disks, but becomes noticeable in dust-rich disks with $\epsilon > 1$, although still modest: growth rates are only halved upon increasing b from zero to unity. This is explained in Appendix A.5 using the one-fluid model of dusty gas.

4.3.2. Viscous Disks

We now consider viscous disks and begin with fixing $\rho_{\rm d}/\rho_{\rm g}$ in Figure 7. In the dust-poor disk with $\rho_{\rm d} = 0.3\rho_{\rm g}$, increasing b has a negligible effect for ${\rm St} \gtrsim 0.1$ and ${\rm St} \lesssim 10^{-2}$, while for intermediate St the SI can persist to slightly higher viscosity with increasing b. However, for $\rho_{\rm d} = 3\rho_{\rm g}$, we find increasing b has noticeable effects: a larger b makes it easier for viscosity to kill the SI and shrinks the region of instability.

We next consider fixing Z. In Figure 8, we show growth rates with $Z = 0.01$ as a function of Stokes number and gas viscosity for different b. Notice the growth rate "gap" shifts from $\epsilon = 1$ for $b = 0$ (see Figure 4) to $\epsilon = 1.4$ for $b = 0.4$ and $\epsilon = 2$ for $b = 1$. This is in fact consistent with the one-fluid model presented in Appendix A.5, for which SI growth rates vanish when $\epsilon = 1 + b$. This explains why the region of "red" SI modes, with dynamical growth rates, shrinks with increasing nonlinearity: at fixed St and increasing α from zero, ϵ drops to $1 + b$ sooner with larger b. We find the maximum allowed viscosity shifts from $\alpha_{\rm max} \sim {\rm St}^{1.5}$ (for $b = 0$) to $\alpha_{\rm max} \sim {\rm St}^{1.6-1.7}$ as b increases, so $\alpha_{\rm max}$ is not sensitive to b. The overall pattern of growth rates does not change significantly as b changes, so nonlinear drag laws have a limited effect.

4.4. Effect of Gas Compressibility

We briefly examine the effect of gas compressibility by varying $\hat{\eta} \equiv \eta R/H_{\rm g}$. For fixed η, that is, the global radial pressure gradient, $\hat{\eta} \propto 1/c_s$. Then larger $\hat{\eta}$ corresponds to smaller c_s, that is, higher compressibility, and vice versa. Thus $\hat{\eta}$ is a measure of gas compressibility (see Youdin & Johansen 2007 and Appendix A.4).

In inviscid disks, the linear SI is unaffected by gas compressibility (Youdin & Goodman 2005). However, for viscous disks, we find SI growth rates increase with gas compressibility. This is shown in Figure 9 where growth rates at fixed metallicities are computed for $\hat{\eta} = 0.01$ and 0.1 (recall our nominal value is 0.05). A comparison between the upper and lower panels indicates that larger compressibility leads to higher growth rates for the same St and α. For instance, in the case with $Z = 0.01$, $\alpha = 10^{-5}$, and ${\rm St} = 10^{-3}$, the growth rate is less than $10^{-6}\Omega$ with $\hat{\eta} = 10^{-2}$, while the growth rate is about $10^{-4}\Omega$ with $\hat{\eta} = 10^{-1}$. This is because diffusion appears as the quantity $\mathcal{D} \equiv \delta/\hat{\eta}^2$ in the dimensionless equations (see Appendix A.4). Thus at fixed δ, increasing $\hat{\eta}$ diminishes the stabilization effect of diffusion.

Similar to the cases in $\hat{\eta} = 0.05$, the differences between the left and right panels of Figure 9 suggest that a larger metallicity expands the dust-rich SI (regions above the black dashed lines, which represent unit ϵ). Although increasing gas compressibility leads to faster growth, we find the maximum allowed α still approximately scales as ${\rm St}^{1.4-1.5}$ (red lines).

It is important to remember our results apply only to the *linear* phase of the instability. In the nonlinear regime, Bai & Stone (2010b) in fact find that increasing η results in weaker particle clumping. This suggests that in reality there is an optimum η that is a balance between linear growth and nonlinear clumping that maximizes planetesimal formation.

5. Application to PPDs

We now apply the above linear theory to global models of PPDs. We first extract the dimensionless input parameters from physical disk models. To do so, we couple classic viscous accretion disk theory (e.g., Pringle 1981) with typical disk profiles used in the literature. We then compute growth timescales and optimum length scales at each radius in order to assess the role of SI in realistic PPDs. Unless otherwise stated, we assume a central star of mass $1M_\odot$ with a Keplerian rotation $\Omega \propto R^{-3/2}$ profile.

We consider the minimum-mass solar nebulae (MMSN) as described in Chiang & Youdin (2010). These disk models have gas surface density and midplane temperature profiles of

$$\Sigma_{\rm g} = 2200F\left(\frac{R}{\rm au}\right)^{-3/2} {\rm g\ cm^{-2}}, \tag{42}$$

$$T = 120\left(\frac{R}{\rm au}\right)^{-3/7} {\rm K}, \tag{43}$$

where F is a scale factor. Assuming vertical hydrostatic equilibrium and a vertically isothermal equation of state, the midplane gas density and pressure scale height profiles are

$$\rho_{\rm g} = 2.7 \times 10^{-9}F\left(\frac{R}{\rm au}\right)^{-39/14} {\rm g\ cm^{-3}}, \tag{44}$$

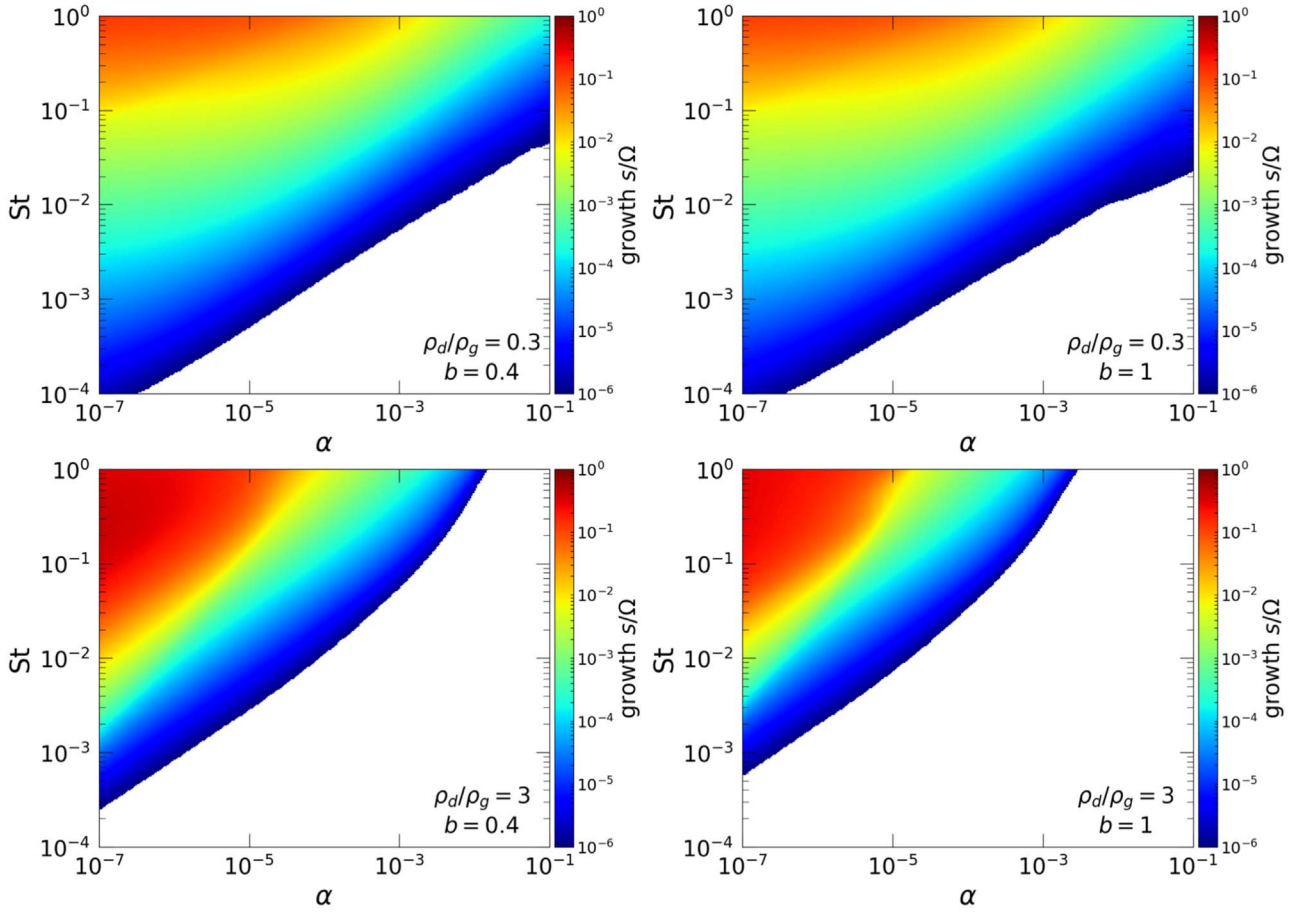

Figure 7. Streaming instability growth rates as a function of Stokes number and viscosity for different degrees of nonlinearity in the dust–gas drag law, as parameterized by b. The top and bottom panels show results for $\epsilon = 0.3$ and $\epsilon = 3$, respectively.

$$H_g = 0.022R\left(\frac{R}{\text{au}}\right)^{2/7}. \tag{45}$$

We assume a constant metallicity, so the dust surface density is given by $\Sigma_d(R) = Z\Sigma_g(R)$.

Using the above model, we can compute global profiles of $\text{St}(R)$, $\hat{\eta}(R)$, $\epsilon(R)$, and $\nu(R)$ as required for linear theory at each radius. We consider a single dust population of a given size and internal density in the Epstein regime. This gives

$$\text{St} = 1.1 \times 10^{-3}F^{-1}\left(\frac{R}{\text{AU}}\right)^{3/2}\left(\frac{\rho_\bullet}{\text{g cm}^{-3}}\right)\left(\frac{a_p}{\text{cm}}\right). \tag{46}$$

Similarly, the dimensionless pressure gradient $\hat{\eta} \equiv \eta R\Omega/c_s$ is

$$\hat{\eta} = 0.035\left(\frac{R}{\text{AU}}\right)^{2/7}. \tag{47}$$

Thus $\hat{\eta}$ is almost a constant.

We also compare the growth timescale with the radial drift timescale of dust particles. The drift timescale is calculated from the radial drift velocity in Equation (19) as

$$\frac{t_{\text{drift}}}{\text{yr}} = \frac{0.73}{F}\left(\frac{R}{\text{AU}}\right)^{17/7} + 5.8 \times 10^5 F(1+\epsilon)^2 \left(\frac{R}{\text{AU}}\right)^{-4/7}, \tag{48}$$

where the midplane dust-to-gas ratio ϵ is calculated according to Equations (24)–(25), which requires a prescription for the disk viscosity (see below). Notice t_{drift} diverges at both small and large radii, as for fixed particle sizes these correspond to $\text{St} \to 0$ and $\text{St} \to \infty$, respectively, which have the slowest drift speeds.

We consider two models of the disk viscosity, $\nu = \alpha c_s H_g$, described below, which are then used to compute H_d/H_g and $\epsilon(R; Z, \text{St}, \alpha)$ from Equations (24) and (25), respectively.

5.1. Accreting Disks

In this case, we assume turbulence leads to (gas) accretion onto the central star, and the viscosity parameter is a measure of turbulent angular momentum transport. Far from the inner disk boundary, we have

$$\nu\Sigma_g \simeq \frac{\dot{M}}{3\pi}, \tag{49}$$

where the (gas) mass accretion $\dot{M}$ is a constant input parameter. For the above gas disk profiles, we obtain

$$\alpha(R) = 8.8 \times 10^{-3}F^{-1}\left(\frac{R}{\text{AU}}\right)^{3/7}\left(\frac{\dot{M}}{10^{-8}M_\odot \text{yr}^{-1}}\right). \tag{50}$$

Thus, higher accretion rates require larger α, while higher disk masses imply smaller α. Note that the viscous accretion flow

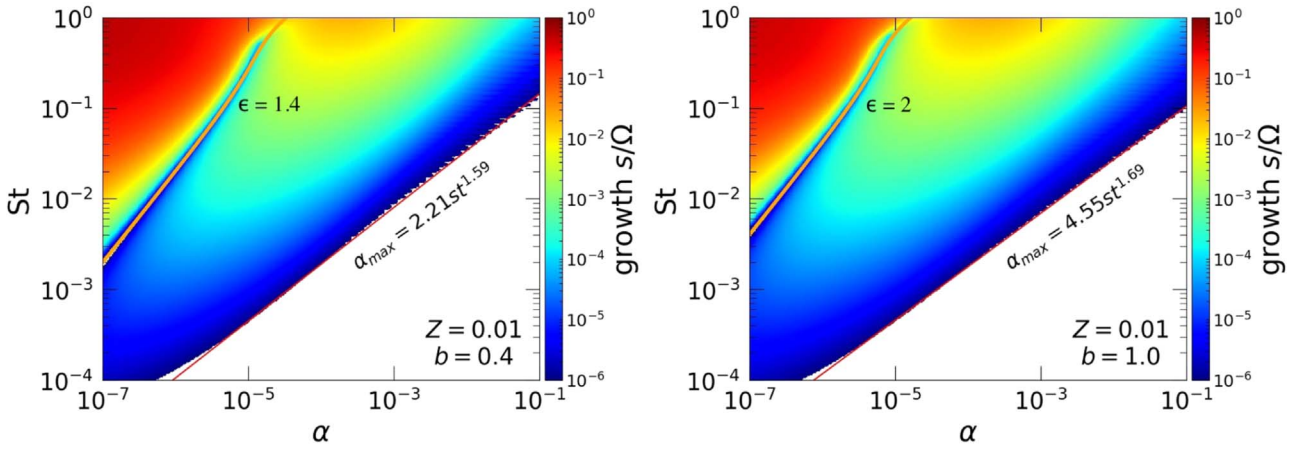

Figure 8. Similar to Figure 7 but for fixed metallicities Z. Orange lines denote $\epsilon = 1 + b$ where the gaps show. Red lines are empirical fits to the maximum allowed α for growth rates to remain $>10^{-6}\Omega$.

has a characteristic radial velocity $\sim\nu/R$, but this is neglected in our local linear analysis.

In Figure 10 we present results for a standard mass accretion rate $\dot{M} = 10^{-8} M_{\odot}\,\mathrm{yr}^{-1}$, disk mass $F = 1$, and centimeter-sized particles with internal density 1 g cm^{-3}. We consider a solar-metallicity disk with $Z = 0.01$ (top) and a dust-enriched disk with $Z = 0.1$ (bottom). We plot growth and dust radial drift timescales (left); Stokes number, midplane dust-to-gas ratios, and α viscosity values (middle); and optimum wavelengths (right).

For both metallicities, growth within the disk lifetime ($\lesssim 10^7$yr) is only possible for $R \gtrsim$ 20–30 au. For $Z = 0.01$, growth timescales $\gtrsim$1Myr at all radii. Increasing Z to 0.1 allows the SI to grow in $\lesssim$1 Myr at a few tens of astronomical units. However, for $Z = 0.1$ we find $\epsilon < 1$ for $R \lesssim 200$ au. This is due to the turbulent stirring by gas, with rather large viscosity values of $\alpha \sim O(10^{-2})$ compared to recent theoretical models (e.g., Bai 2015; Simon et al. 2018) and measurements of disk turbulence (Flaherty et al. 2017, 2018). It is doubtful that such dust-poor conditions can lead to planetesimal formation in the nonlinear regime of the SI (Johansen et al. 2009). Furthermore, radial drift timescales in these regions are shorter than the growth time, implying dust may be lost to the star before significant growth.

On the other hand, we find $t_{\rm SI} \lesssim t_{\rm drift}$ for $R \gtrsim 400$ au for $Z = 0.01$ and for $R \gtrsim 100$ au for $Z = 0.1$, suggesting that dust in the outer disk can undergo efficient SI before falling into the host star. There is, however, some uncertainty because in these regions St $\gtrsim 1$, which violates the fluid treatment of dust.

We find characteristic SI length scales are of $O(10H_{\rm g})$ in both cases. This is problematic in two respects. At $\sim$100 au, the gas disk aspect ratio is $H_{\rm g}/R \sim 0.08$, implying a radial length scale comparable to the disk radius, $\lambda_x \sim 8H_{\rm g} \sim R$. At this scale, the global disk geometry may become important, but this is neglected in our local stability analyses. Moreover, we find that the vertical length scales are much larger than the dust scale height, $\lambda_z \gg H_{\rm g} \gg H_{\rm d}$. The existence of such vertically extended modes may then depend on physical conditions at the surface of the dust layers. This issue is beyond the scope of this work.

5.2. Nonaccreting Disks

These disk models may be considered as representing "dead zones" in PPDs, where weak turbulence results from hydrodynamic instabilities but does not contribute to mass accretion (Bai 2016). Thus we require $\nu \neq 0$, but without a corresponding radial gas flow ($v_R = 0$). This is in fact consistent with our local models. Since we have chosen MMSN surface density profiles, we deduce the appropriate viscosity profile as follows. It turns out these disks have almost a constant α that may be specified independently.

We recall from classic viscous theory that the (gas) radial velocity is given via

$$R\Sigma_{\rm g} v_R \frac{d}{dR}(R^2\Omega) = \frac{d}{dR}\left(R^3 \nu \Sigma_{\rm g} \frac{d\Omega}{dR}\right). \tag{51}$$

(Note that this equation is also applicable to unsteady disks.) For a Keplerian disk, we obtain

$$v_R = -\frac{3}{\sqrt{R}\Sigma_{\rm g}} \frac{d}{dR}(\nu \Sigma_{\rm g} \sqrt{R}). \tag{52}$$

Thus, if $\nu\Sigma_{\rm g}\sqrt{R}$ is constant, then $v_R = 0$. Such nonaccreting disks have also been employed in other problems, for example, disk–planet interaction (Paardekooper & Papaloizou 2009). We use the above constraint to set

$$\alpha(R) = \alpha_1 \left(\frac{R}{\rm AU}\right)^{-1/14}, \tag{53}$$

where α_1 is the viscosity coefficient at 1au and is an input parameter.

Figure 11 shows example results in nonaccreting disks. Here, we fix $\alpha_1 = 10^{-3}$. We find that the SI can grow within the disk lifetime for $R \gtrsim 3$ au, much smaller than in the accreting disks. This is due to the smaller viscosity compared to the nonaccreting disk above. However, as in accreting disks, the SI grows fastest at $R \sim 100$ au.

For $Z = 0.01$, we find $\epsilon \lesssim 1$ for $R \lesssim 100$ au. Here, the linear SI grows sufficiently fast, but ϵ is insufficient for dust clumping (Johansen et al. 2009). Thus we only expect the development of axisymmetric dust rings.

On the other hand, in the $Z = 0.1$ disk we find $\epsilon \gtrsim 1$ for $R \gtrsim 20$ au, and growth timescales are much shorter than the disk lifetime. In this case, the SI will likely lead to planetesimal

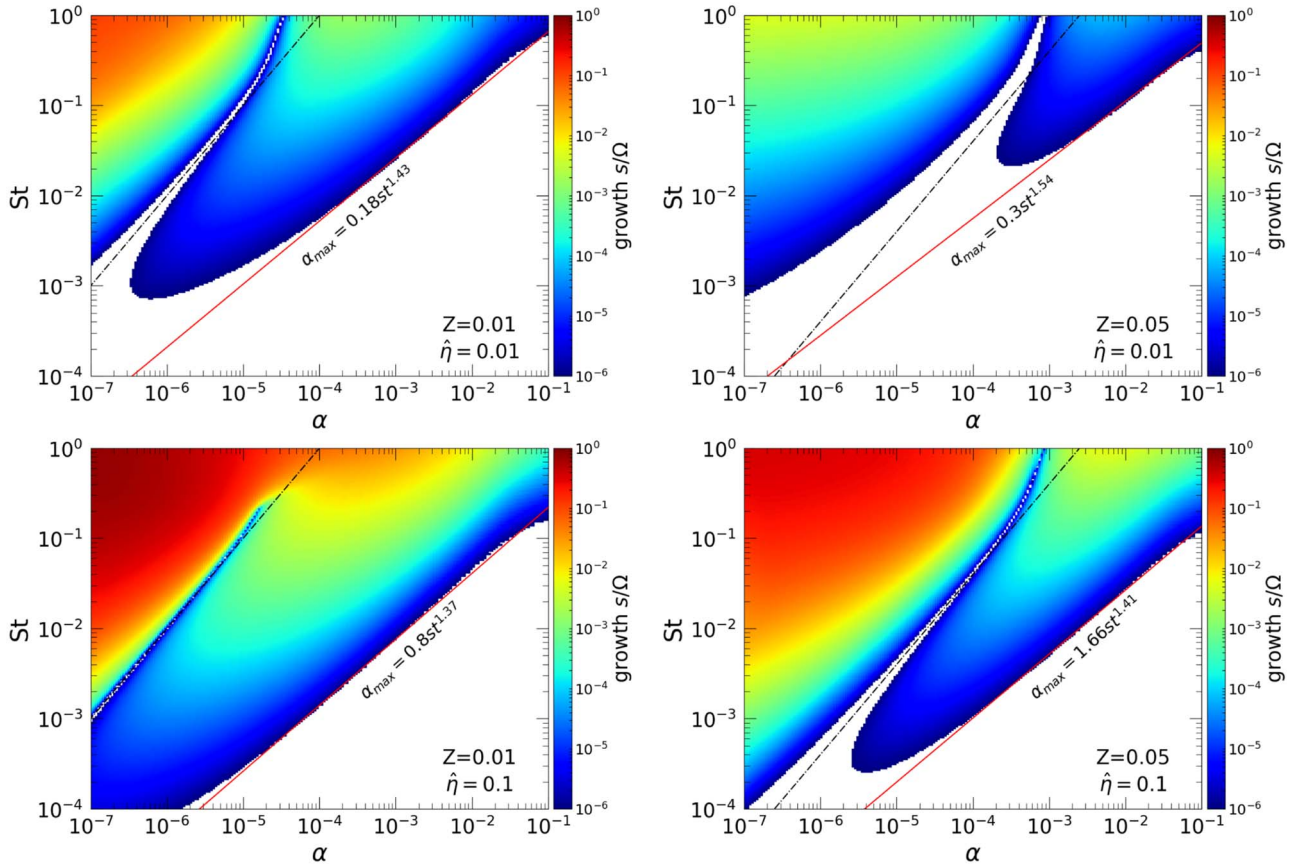

Figure 9. Growth rates of the streaming instability at fixed metallicity for different levels of gas compressibility, as measured by $\hat{\eta} = 0.01$ (upper panels) and $\hat{\eta} = 0.1$ (lower panels). The black dotted–dashed lines in each panel correspond to Equation (41). Red lines are empirical fits to the maximum allowed α for growth rates to remain $>10^{-6}\Omega$.

formation. The sudden increase of $t_{\rm SI}$ at $R \sim 20$ au is associated with ϵ approaching unity, whence SI is quenched (see, e.g., Appendix A.5).

In both cases, comparisons between radial drift timescales (black) and SI growth timescales (red) are also shown. We find $t_{\rm SI} \lesssim t_{\rm drift}$ beyond 10 au and 30 au for $Z = 0.01$ and $Z = 0.1$, respectively. Here the SI can grow before dust particles are lost to the star. Conversely, interior to these radii, SI is limited by radial drift instead of disk lifetimes.

In either disk model, we find $\lambda_x \sim H_{\rm g} \ll R$ at $R = 100$ au, which is consistent with the local analysis. However, vertical wavelengths are still significantly larger than $H_{\rm d}$. We have attempted to restrict $\lambda_z \leqslant 2H_{\rm d}$ (the full dust layer thickness) for self-consistency, but this in fact leads to growth timescales exceeding the disk lifetime. This is because viscosity is effective in stabilizing perturbations with such small vertical length scales.

5.3. Dust Rings around HL Tau

We now apply the above disk models to examine whether or not the SI can explain the formation of the dust rings and gaps observed in the PPD around HL Tau (ALMA Partnership et al. 2015). These dust rings are located between ∼13 and ∼91 au, and adjacent rings are separated by ∼10–20 au. We require growth timescales $\lesssim$1Myr for consistency with HL Tau's young age. Because the disk mass of HL Tau is about $0.1M_\odot$ (ALMA Partnership et al. 2015), which is about 10 times larger than MMSN, we adopt $F = 10$ in the calculations below. We still consider centimeter-sized particles with internal density 1 g cm^{-3}. Calculations with millimeter-sized particles yield essentially no growth within the disk's age.

For the accreting disk model, we adopt $\dot{M} \sim 10^{-7}M_\odot{\rm yr}^{-1}$ (Beck et al. 2010). However, this implies a high viscosity, with α increasing from $\sim 10^{-2}$ at 1 au to ∼0.07 at 100 au. As a result, SI growth timescales exceed 100 Myr. We thus discard this model.

For the nonaccreting disk model, we set $\alpha_1 = 10^{-4}$. This is motivated by the estimate made by Pinte et al. (2016) based on observational constraints on the dust layer thickness in the HL Tau disk. Results are shown for $Z = 0.01$ and 0.1 in Figure 12. For both cases, the fastest growth occurs near the outer disk edge ∼100 au. Notice here that radial drift does not limit the instability growth. (For $Z = 0.1$, $t_{\rm drift}$ exceeds a million years, so it is outside the plotted range.)

For $Z = 0.01$, we find $t_{\rm SI} \lesssim$ 1Myr beyond ∼15 au. In these regions, the MMSN profile gives $H_{\rm g} \simeq 0.7$ au at $R = 15$ au. Here, the radial wavelength is $10H_{\rm g} = 7$ au, which is too small compared to the observed ring separations. By contrast, at 100 au the radial wavelength is $\simeq 2H_{\rm g} = 16$ au, which is broadly consistent with observations. In the $Z = 0.1$ disk, we find SI only grows sufficiently fast for $R \gtrsim 50$ au. However, at these radii, the radial wavelengths range between 6.7 au at 50 au to 1.6 au at 100 au, which are too small compared to observations.

From the above crude comparison, we conclude that the $Z = 0.01$ disk can plausibly explain dust rings observed in the outer disk ($R \gtrsim 70$ au where $\lambda_x \gtrsim 10$ au). However, we again find $\lambda_z \gg H_{\rm d}$. Additional calculations enforcing $\lambda_z \leqslant 2H_{\rm d}$ resulted in decaying modes, which would play no role.

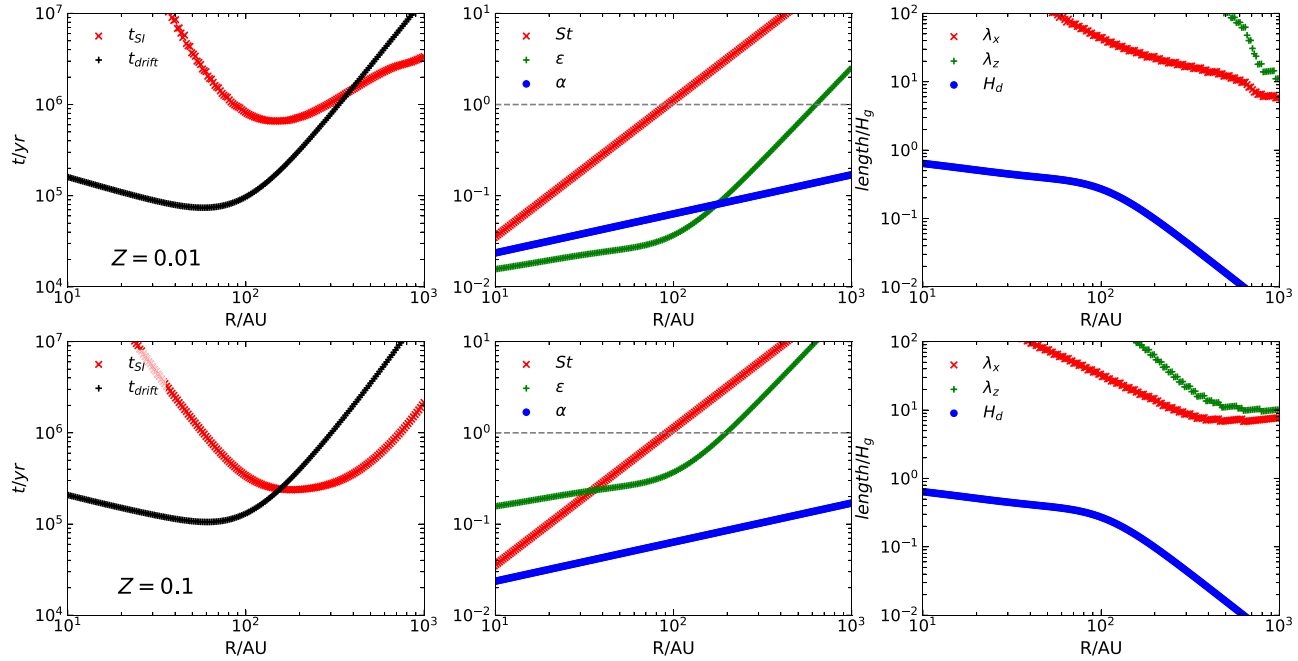

Figure 10. Streaming instability as a function of radius in a minimum-mass solar nebula accreting PPD. The left panel shows growth $t_{\rm SI}$ (red) and radial drift timescales $t_{\rm drift}$ (black); the middle panel shows the Stokes number St (red), midplane dust-to-gas ratio ϵ (green), and viscosity α (blue); and the right panel shows the radial and vertical wavelengths $\lambda_{x,z}$ (red, green) of the SI mode, in comparison with the dust scale height $H_{\rm d}$ (blue). The horizontal dashed lines indicate St $= 1$ and $\epsilon = 1$.

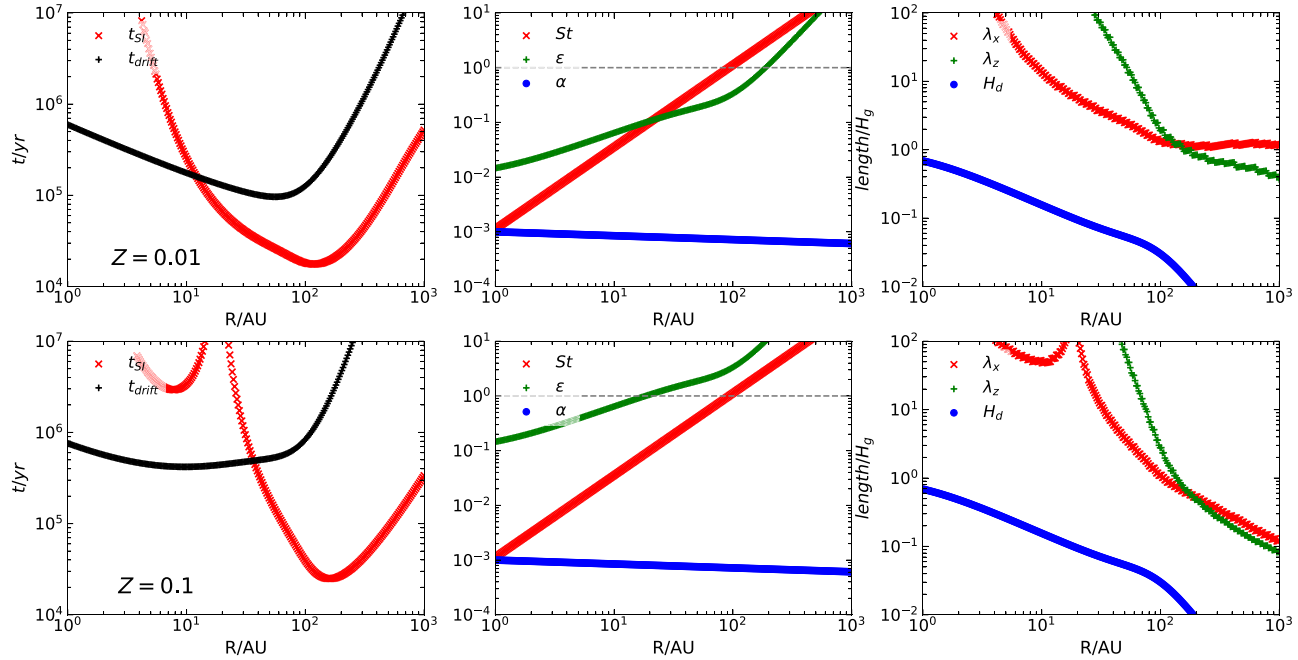

Figure 11. Same as Figure 10 but for nonaccreting disks parameterized by $\alpha_{\rm l} = 10^{-3}$.

In any case, because $\epsilon \lesssim 1$ in the $Z = 0.01$ disk model, SI is unlikely to result in planetesimal formation. This would suggest that planetesimals cannot form via the SI in the HL Tau disk, leaving only axisymmetric rings from the instability.

6. Summary and Discussion

In this paper, we assess the efficiency of planetesimal formation via the streaming instability (SI) in physical models of PPDs. To this end, we generalize the linear theory of the SI to include disk turbulence, modeled as a gas viscosity, with a corresponding particle stirring modeled by dust diffusion. We also explore the modest effect of nonlinear drag laws and gas compressibility on the SI. For the most part, we adopt the standard two-fluid model of dusty gas, but we also verify some calculations with a simplified, one-fluid model generalized from Lin & Youdin (2017) to include dust diffusion.

We find the SI is sensitive to turbulence. Gas viscosity and particle diffusion stabilize the SI and increase its characteristic length scale, as expected on physical grounds. SI with small

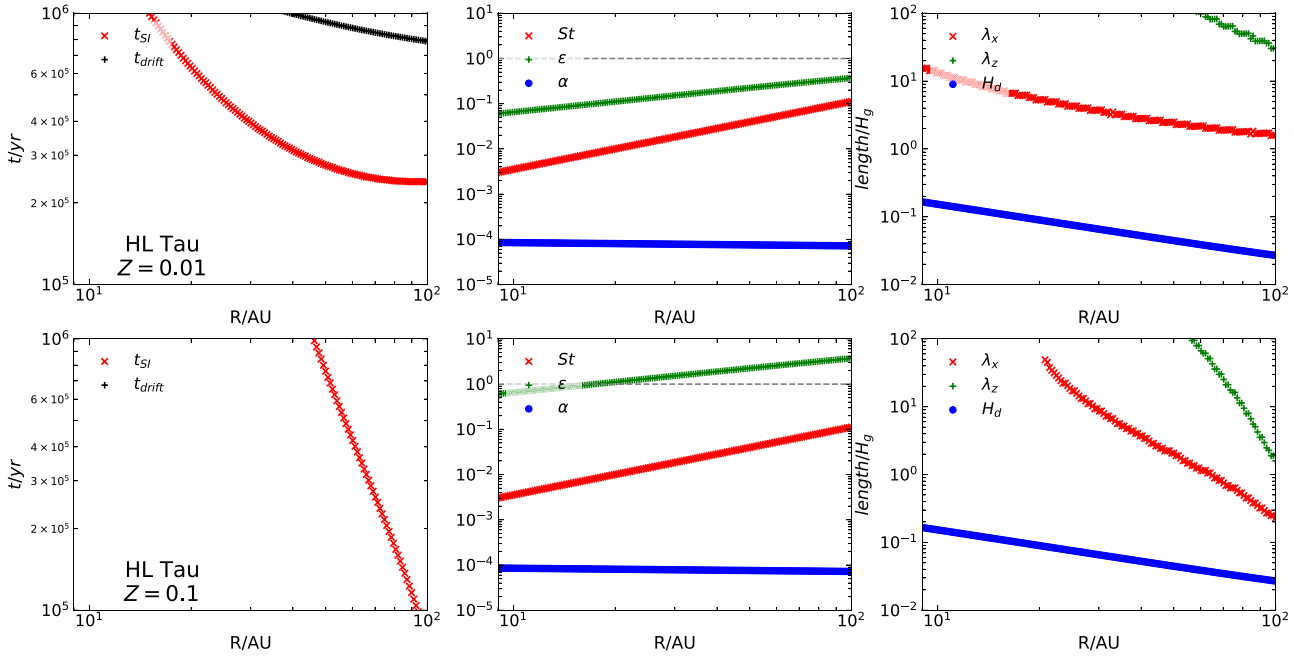

Figure 12. Streaming instability in the PPD around HL Tau, based on the nonaccreting disk model.

particles is effectively stabilized by turbulence. For example, at fixed dust-to-gas ratios for St $\sim 10^{-2}$, growth rates become negligible for $\alpha \gtrsim 10^{-3}$. We also find the SI is more easily smeared out in the vertical direction than in the radial direction, consistent with Umurhan et al. (2019).

In a physical disk, however, turbulence also changes the background disk structure, namely the equilibrium dust-to-gas ratio. Accounting for this yields two regimes: at low viscosity the dust-to-gas ratio exceeds unity and the SI grows on dynamical timescales, and at high viscosity the dust-to-gas ratio falls below unity and the SI grows slowly, eventually exceeding the timescales of interest. Our numerical results indicate a convenient scaling for the maximum viscosity as $\alpha_{\max} \sim \mathrm{St}^{1.5}$.

We apply a linear stability analysis to global models of PPDs. We consider the standard minimum-mass solar nebula disk models with viscosity either chosen to yield a specified global gas accretion rate or set independently in a nonaccreting disk. Even considering large, centimeter-sized particles that should favor the SI, we find the SI only grows within typical disk lifetimes of a few megayears outside ∼10 au. The SI is most efficient around 100 au, where growth timescales can approach $O(10^4)$ yr at low viscosity.

On the other hand, we consistently find that the vertical length scales of the SI exceed the dust layer thickness. Taken at face value, this suggests that in viscous disks the SI has little vertical structure across the dust layer. However, only a stratified linear stability analysis can confirm whether not there exists vertically unstructured modes or modes that can be confined to the dust layer (M.-K. Lin et al. 2020, in preparation).

Our local analyses also neglect the viscosity-induced gas accretion flow that exists in global disks. Future work should account for this by calculating the background equilibrium flow self-consistently. This gas accretion flow would drive an additional relative drift between dust and gas on top of that due to dust–gas drag. As the relative dust–gas drift is the culprit of dust–gas instabilities, including the SI (Squire & Hopkins 2018), we can expect a gas accretion flow to also affect the SI. We leave this to future work.

We thank the anonymous referee for a prompt and clear report that helped to improve the communication of results. This work is supported by the Taiwan Ministry of Science and Education (grant 107-2112-M001-043-MY3) and the ASIAA Summer Student Program. We thank O. Umurhan for useful discussions.

Appendix
One-fluid Model for Dusty Gas with Particle Diffusion

Here we describe the "one-fluid" model of dusty gas developed by Lin & Youdin (2017), based on the earlier studies of Laibe & Price (2014) and Price & Laibe (2015). We extend these models by including dust diffusion, but we neglect gas viscosity for simplicity (see Lovascio & Paardekooper 2019 for a viscous but diffusionless version of the one-fluid model).

In this description, one forgoes separate gas and dusty variables and works with the total density

$$\rho \equiv \rho_{\rm d} + \rho_{\rm g} \tag{54}$$

and the center-of-mass velocity of the mixture

$$\boldsymbol{U} \equiv \frac{\rho_{\rm d}\boldsymbol{W} + \rho_{\rm g}\boldsymbol{V}}{\rho}. \tag{55}$$

Furthermore, by considering small particles, one applies the "terminal velocity approximation" (Youdin & Goodman 2005; Jacquet et al. 2011) so that

$$\boldsymbol{W} - \boldsymbol{V} = \frac{\nabla P}{\rho_{\rm g}} t_{\rm s}, \tag{56}$$

where $t_{\rm s} \equiv \tau_{\rm s} f_{\rm g}$ is the relative stopping time and $f_{\rm g} = \rho_{\rm g}/\rho_{\rm g}$ is the gas fraction. (It is simpler to work with $t_{\rm s}$ in the one-fluid framework.) As before, we consider strictly isothermal gas so

that $P = c_s^2 \rho_g = c_s^2 (1 - f_d)\rho$, where $f_d = \rho_d/\rho$ is the dust fraction.

With the above definitions and approximations, the two-fluid Equations (1)–(4) can be combined and simplified to give

$$\frac{\partial \rho}{\partial t} + \nabla \cdot (\rho \boldsymbol{U}) = \nabla \cdot \left[DP \nabla \left(\frac{\rho}{P} \right) \right], \tag{57}$$

$$\frac{\partial \boldsymbol{U}}{\partial t} + \boldsymbol{U} \cdot \nabla \boldsymbol{U} = -\frac{1}{\rho} \nabla P - \Omega_K^2 R \hat{\boldsymbol{R}} \tag{58}$$

$$\frac{\partial P}{\partial t} + \boldsymbol{U} \cdot \nabla P = -P \nabla \cdot \boldsymbol{U} + c_s^2 \nabla \cdot (t_s f_d \nabla P). \tag{59}$$

Note that only three of the four evolutionary equations remain because the dust velocity has been eliminated with the terminal velocity approximation. Equation (59) is an effective energy equation that results from the dust continuity Equation (2). Terms of $O(t_s^2)$ are neglected because of the assumption of small particles. For the following derivations, it is convenient to define

$$\mathcal{C} \equiv c_s^2 \nabla \cdot (t_s f_d \nabla P) = -c_s^2 \nabla \cdot (\rho t_s f_d \boldsymbol{F}), \tag{60}$$

$$\boldsymbol{F} \equiv -\frac{\nabla P}{\rho}. \tag{61}$$

A.1. Relative Stopping Time

We adopt the same stopping-time parameterization as the two-fluid model (Equation (14)). The corresponding definition of the relative stopping time is

$$t_s = t_{s,eqm} \frac{[\rho \rho_g^{a-1} |\boldsymbol{W} - \boldsymbol{V}|^b]_{eqm}}{\rho \rho_g^{a-1} |\boldsymbol{W} - \boldsymbol{V}|^b}. \tag{62}$$

Combining Equation (56) with Equation (62) gives

$$|\boldsymbol{W} - \boldsymbol{V}|^{1+b} = t_{s,eqm} [\rho_g^{a-1} \rho |\boldsymbol{W} - \boldsymbol{V}|^b]_{eqm} \frac{1}{\rho_g^a} \left| \frac{\nabla P}{\rho} \right|. \tag{63}$$

It will prove useful to have an expression for ρt_s. Using Equation (63), we find

$$\ln (\rho t_s) = \left(1 - \frac{a}{1+b} \right) \ln \rho_g - \frac{b}{1+b} \ln \left| \frac{\nabla P}{\rho} \right| + \text{const.} \tag{64}$$

A.2. One-fluid Equilibrium

The one-fluid momentum equations admit axisymmetric, steady-state equilibrium solutions with $U_R = U_Z = 0$, and

$$U_\phi^2 = R^2 \Omega_K^2(R) + \frac{R}{\rho} \frac{\partial P}{\partial R}, \tag{65}$$

$$= R^2 \Omega_K^2 (1 - 2 f_g \eta). \tag{66}$$

Because $\eta \ll 1$, we can set $U_\phi = R\Omega_K$ in practice.

The steady-state continuity and effective energy Equations (57) and (59) are generally not satisfied for arbitrary density and pressure profiles. However, if we consider power-law disks where the density and pressure vary on a global scale $\partial_R \sim 1/R$, then the effective energy equation implies the background would evolve on a timescale of $O(1/h^2 \mathrm{St} \Omega_K)$, where $h \ll 1$ is the disk aspect ratio. Similarly, the continuity equation gives a background evolution timescale of $O(1/\delta h^2 \Omega_K)$. These timescales are much longer than the SI growth timescales found below. We can thus self-consistently neglect the background evolution.

A.3. Linearized One-fluid Equations

As in the main text, we consider axisymmetric Eulerian perturbations with spacetime dependence $\exp(\sigma t + k_x R + k_z z)$ and linearize Equations (57)–(59). We assume the radial wavenumbers $|k_x R| \gg 1$ so that background density and pressure gradients may be neglected when compared to that in the perturbed variables. We find

$$\sigma \frac{\delta \rho}{\rho} = -\mathrm{i} k_x \delta U_R - \mathrm{i} k_z \delta U_z - D k^2 \left[\frac{\delta \rho}{\rho} - (1 + \epsilon) \frac{\delta P}{c_s^2 \rho} \right], \tag{67}$$

$$\sigma \delta U_R = 2\Omega \delta U_\phi + \delta F_R, \tag{68}$$

$$\sigma \delta U_\phi = -\frac{\Omega}{2} \delta U_R, \tag{69}$$

$$\sigma \delta U_z = -\mathrm{i} k_z \frac{\delta P}{\rho} \tag{70}$$

$$\sigma \frac{\delta P}{\rho} = -\frac{P}{\rho} (\mathrm{i} k_x \delta U_R + \mathrm{i} k_z \delta U_z) + \frac{\delta \mathcal{C}}{\rho}, \tag{71}$$

where $k^2 = k_x^2 + k_z^2$ and

$$\delta F_R = -F_R \frac{\delta \rho}{\rho} - \mathrm{i} k_x \frac{\delta P}{\rho}. \tag{72}$$

The linearized diffusive term is

$$-\frac{\delta \mathcal{C}}{c_s^2 \rho} = \mathrm{i} k_x F_R t_s \left[f_g \frac{\delta \rho}{\rho} - \frac{1}{c_s^2} \frac{\delta P}{\rho} + f_d \frac{\delta (\rho t_s)}{\rho t_s} \right] + t_s f_d \left[(k_x^2 + k_z^2) \frac{\delta P}{\rho} - \mathrm{i} k_x F_R \frac{\delta \rho}{\rho} \right], \tag{73}$$

and linearizing Equation (64) gives

$$\frac{\delta (\rho t_s)}{\rho t_s} = \frac{1}{f_g c_s^2} \left(1 - \frac{a}{1+b} \right) \frac{\delta P}{\rho} - \frac{b}{1+b} \frac{\delta F_R}{F_R}. \tag{74}$$

The full expression for $\delta \mathcal{C}$ is then

$$-\frac{\delta \mathcal{C}}{\rho c_s^2} = \mathrm{i} k_x F_R t_s \left(f_g - \frac{f_d}{1+b} \right) \frac{\delta \rho}{\rho} + t_s \left[\frac{\mathrm{i} k_x F_R}{c_s^2} \theta + f_d \left(k^2 - \frac{b k_x^2}{1+b} \right) \right] \frac{\delta P}{\rho},$$

where

$$\theta \equiv \epsilon \left(1 - \frac{a}{1+b} \right) - 1. \tag{75}$$

In Figure 13 we compare growth rates from the full two-fluid equations and the one-fluid model. We consider Epstein drag with $a = 1, b = 0$. For the two-fluid model, we include particle diffusion but neglect gas viscosity. We also use the optimum wavenumbers found in the two-fluid model in the one-fluid calculation. We find the one-fluid model is consistent

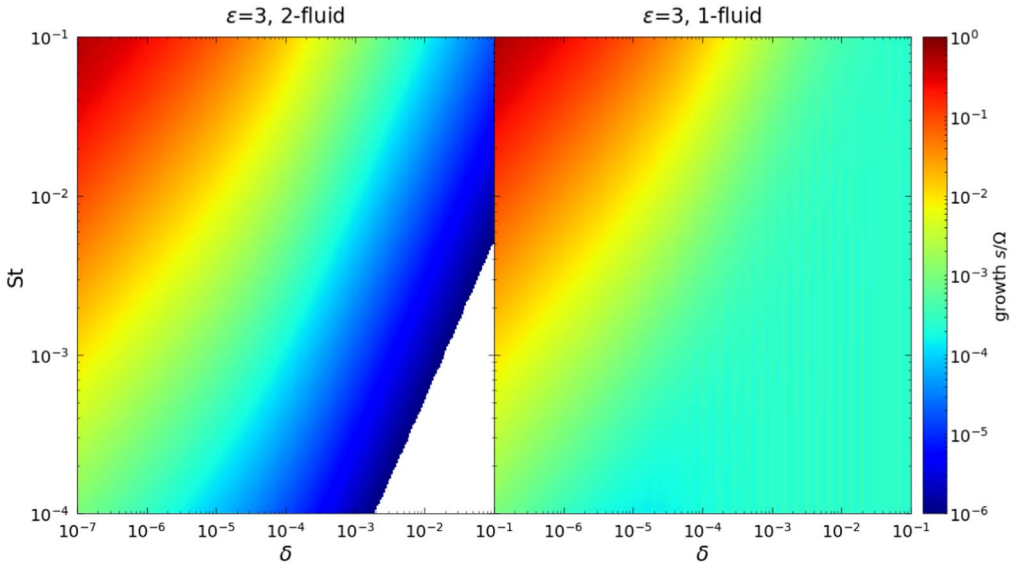

Figure 13. Growth rates as a function of Stokes number St and dust diffusion δ computed from the two-fluid (left) and one-fluid (right) models. The optimal K_x and K_z values found in the two-fluid model are used in the one-fluid model. Plots are truncated if growth rates are smaller than $10^{-6}\Omega$.

with the two-fluid model when diffusion is weak with $\delta \lesssim 10^{-4}$. The one-fluid framework produces spuriously growing modes for larger δ, although their growth rates remain small.

A.4. Reduced Model

We can simplify the linearized one-fluid equations to obtain a reduced dispersion relation. It is convenient to first render the one-fluid equations dimensionless by adopting dimensionless parameters $\mathrm{St} = \tau_s\Omega$, $K_{x,z} = \eta R k_{x,z}$ as used in the main text. (Recall the Stokes number St is defined via the particle stopping time $\tau_s = t_s/f_g$.) We further introduce the dimensionless variables

$$n \equiv \mathrm{i}\sigma/\Omega, \quad \mathcal{D} \equiv \frac{D}{(\eta R)^2\Omega}. \tag{76}$$

Note that the dimensionless diffusion coefficient used in the main text is given by $\delta \equiv D/c_s H_g = \mathcal{D}\hat{\eta}^2$.

We eliminate the velocity perturbations from Equations (67)–(71) to obtain

$$\left\{\zeta_1(\mathrm{i}n - \mathcal{D}K^2) - \mathrm{St}f_g\left[\frac{f_d}{\hat{\eta}^2}\left(K^2 - \frac{bK_x^2}{1+b}\right) + 2\zeta_1\mathrm{i}K_x f_g\,\theta\right]\right\} \times \frac{\delta P}{c_s^2\rho} = f_g\left[(\mathrm{i}n - \mathcal{D}K^2) + 2\mathrm{i}K_x f_g\,\mathrm{St}\left(f_g - \frac{f_d}{1+b}\right)\right]\frac{\delta\rho}{\rho}, \tag{77}$$

$$\{n^2[(\zeta_2 n^2 - 1) + 2\mathrm{i}K_x f_g] + \mathrm{i}n(n^2-1)\mathcal{D}K^2\}\frac{\delta\rho}{\rho} = \left[\frac{1}{\hat{\eta}^2}(n^2K^2 - K_z^2) + \mathrm{i}\zeta_1 n(n^2-1)(1+\epsilon)\mathcal{D}K^2\right]\frac{\delta P}{c_s^2\rho}, \tag{78}$$

where we have used the definition $F_R = 2f_g\eta R\Omega_K^2$, and recall $\hat{\eta} = \eta R\Omega_K/c_s$. The artificial coefficients $\zeta_{1,2}$ are nominally unity but are inserted to make the following simplifications:

1. We consider incompressible gas with $\hat{\eta} \ll 1$. This is equivalent to setting $\zeta_1 \to 0$. Note that this removes the dependence on the gas density via the drag law.
2. We consider low-frequency modes with $|n| \ll 1$. This is equivalent to setting $\zeta_2 \to 0$.

These approximations give the dispersion relation

$$(1 + f_d\,\mathrm{St}\mathcal{D}K^2 b')n^3 + [\mathrm{i}(f_d\,\mathrm{St}b' + \mathcal{D}K^2) + 2K_x f_g\,\mathrm{St} \times \left(1 - \frac{f_d}{1+b} - \frac{bf_d}{1+b}\frac{K_x^2}{K^2}\right)]n^2 - \left(f_d\,\mathrm{St}\mathcal{D}K^2 b' + \frac{K_z^2}{K^2}\right)n + \left[2f_g K_x\,\mathrm{St}\left(\frac{f_d}{1+b} - f_g\right) - \mathrm{i}\mathcal{D}K^2\right]\frac{K_z^2}{K^2} = 0, \tag{79}$$

where

$$b' \equiv 1 - \frac{b}{1+b}\frac{K_x^2}{K^2}. \tag{80}$$

Note that for fixed δ we also require $\delta \ll \min[\mathrm{St}f_d f_g, |n - K_z^2/nK^2|/(1+\epsilon)]$. Equation (79) agrees with Equation (97) of Lin & Youdin (2017) in the diffusionless limit with Epstein drag ($\mathcal{D} = b = 0$) and $|n| \ll 1$. The latter dispersion relation was also derived by Jacquet et al. (2011) and Laibe & Price (2014) and is consistent with the original SI analysis of YG05.

Figure 14 compares the growth rates from this reduced model (Equation (79)) and the full two-fluid equations as a function of St for $\delta = 10^{-4}$, 10^{-5}, and 10^{-6}. We fix $\rho_d/\rho_g = 3$. We use the optimum K_x and K_z from the two-fluid model when solving Equation (79). We obtain excellent agreement with the two-fluid model for weak diffusion, $\delta \leqslant 10^{-5}$. Even for relatively large $\delta = 10^{-4}$ the curves are similar. We remark that the incompressible approximation filters out spurious modes in the one-fluid equations that appear at large δ and small St (i.e., the lower right part of the right panel in Figure 13).

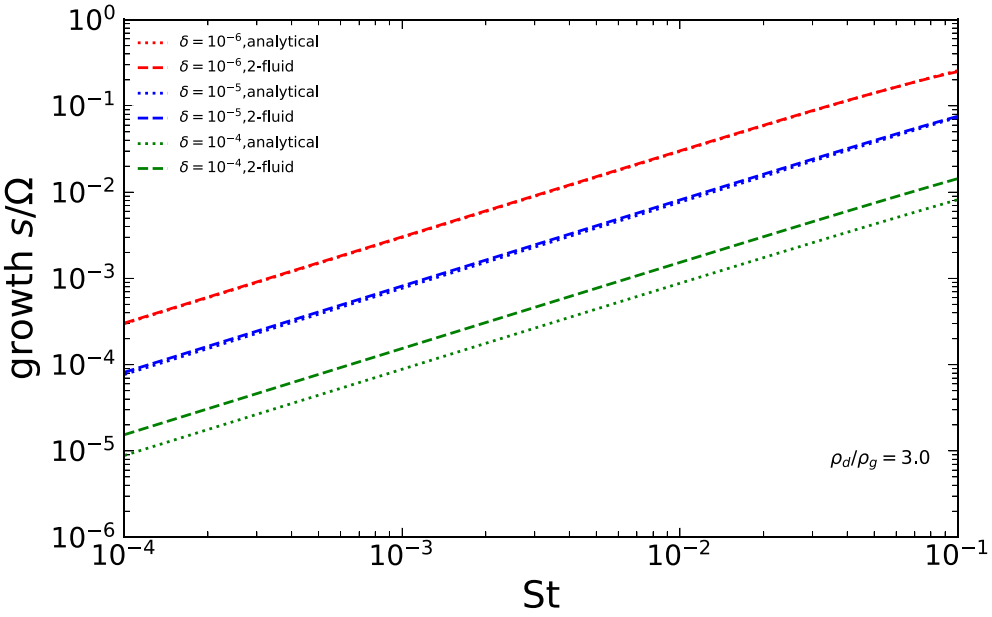

Figure 14. Growth rates of the analytical model (Equation (79)) and the full two-fluid model with dust-to-gas ratio $\epsilon = 3$ as a function of Stokes numbers for different strengths of particle diffusion. We use the optimum values of K_x and K_z found by the two-fluid model in both calculations.

A.5. Dust-rich, Diffusionless Solutions

We can obtain closed-form solutions to Equation (79) in the limit of vanishing dust diffusion. We fix K_z, f_d and maximize growth rates over K_x, assuming that the optimum K_x is large. (This in turn implies a small stopping time.) Thus we replace $K^2 \to K_x^2$.

As a simplification, we neglect the quadratic term in Equation (79). This is consistent with the final solution obtained below if

$$f_d \gg \frac{12(b+1)}{12b+17}. \tag{81}$$

Although this can only be marginally satisfied (since $f_d < 1$), we find this approximation nevertheless give the correct growth rates.

Deleting the quadratic term Equation (79), we solve the depressed cubic

$$n^3 - \mathcal{P}n = \mathcal{Q}, \tag{82}$$

where the coefficients $\mathcal{P}$, $\mathcal{Q}$ can be read off Equation (79) with $\mathcal{D} = 0$. Writing $n = \mu + \mathcal{P}/3\mu$, we obtain a quadratic for μ^3:

$$\mu^6 - \mu^3 + \frac{\mathcal{P}^3}{27} = 0. \tag{83}$$

It turns out the last term may be effectively neglected (Lin & Youdin 2017, their Appendix D2), so $\mu \simeq \mathcal{Q}^{1/3}$. This gives

$$\mathrm{Re}(n) = \frac{1}{2}(\mathcal{A}\mathrm{St}^{1/3}K_x^{-1/3} + \mathcal{B}\mathrm{St}^{-1/3}K_x^{-5/3}),$$

$$\mathrm{Im}(n) = \frac{\sqrt{3}}{2}(\mathcal{A}\mathrm{St}^{1/3}K_x^{-1/3} - \mathcal{B}\mathrm{St}^{-1/3}K_x^{-5/3}),$$

$$\mathcal{A} = \left[2f_g\left(\frac{b+2}{b+1}f_d - 1\right)K_z^2\right]^{1/3},$$

$$\mathcal{B} = \frac{K_z^2}{3\mathcal{A}}.$$

We maximize growth rates $\mathrm{Im}(n)$ over K_x. Denoting the associated quantities with $*$, we find

$$\mathrm{Im}(n_*) = \frac{2}{\sqrt{5}}\left(\frac{3}{5}\right)^{3/4}\sqrt{2K_z\mathrm{St}f_g\left(\frac{b+2}{b+1}f_d - 1\right)}, \tag{84}$$

$$\mathrm{Re}(n_*) = \frac{\sqrt{3}}{2}\mathrm{Im}(n_*), \tag{85}$$

$$K_{x,*} = \frac{2}{\sqrt{5}}\frac{K_z}{\mathrm{Im}(n_*)}. \tag{86}$$

The maximum growth rate in Equation (84) generalizes Equation (111) of Lin & Youdin (2017) to nonlinear drag laws. Growth rates vanish when $f_d = (b+1)/(b+2)$, which is equivalent to $\epsilon = 1 + b$. This can also be seen from Equation (79): in the diffusionless limit when $\epsilon = 1 + b$, the last term vanishes and the dispersion relation reduces to a quadratic in n. From Equation (84) we find

$$\frac{\partial\,\mathrm{Im}(n_*)}{\partial b} = -\frac{f_d\,\mathrm{Im}(n_*)}{2(b+1)[(b+2)f_d - (b+1)]}. \tag{87}$$

Hence, for growing modes with $\mathrm{Im}(n_*) > 0$, increasing b tends to stabilize modes. The effect is small because $\mathrm{Im}(n_*)$ only depends on b through $(b+2)/(b+1)$, which ranges between one and two for $b = 0$ to ∞ (see Equation (84)).

ORCID iDs

Min-Kai Lin https://orcid.org/0000-0002-8597-4386

References

ALMA Partnership, Brogan, C. L., Pérez, L. M., et al. 2015, ApJL, 808, L3
Armitage, P. J., Eisner, J. A., & Simon, J. B. 2016, ApJL, 828, L2
Auffinger, J., & Laibe, G. 2018, MNRAS, 473, 796
Bai, X.-N. 2015, ApJ, 798, 84
Bai, X.-N. 2016, ApJ, 821, 80
Bai, X.-N., & Stone, J. M. 2010a, ApJ, 722, 1437
Bai, X.-N., & Stone, J. M. 2010b, ApJL, 722, L220

Balbus, S. A., & Hawley, J. F. 1991, ApJ, 376, 214
Balsara, D. S., Tilley, D. A., Rettig, T., & Brittain, S. D. 2009, MNRAS, 397, 24
Beck, T. L., Bary, J. S., & McGregor, P. J. 2010, ApJ, 722, 1360
Birnstiel, T., Dullemond, C. P., & Brauer, F. 2010, A&A, 513, A79
Blum, J. 2018, SSRv, 214, 52
Carrera, D., Gorti, U., Johansen, A., & Davies, M. B. 2017, ApJ, 839, 16
Carrera, D., Johansen, A., & Davies, M. B. 2015, A&A, 579, A43
Chiang, E., & Youdin, A. N. 2010, AREPS, 38, 493
Drążkowska, J., Alibert, Y., & Moore, B. 2016, A&A, 594, A105
Drążkowska, J., & Dullemond, C. P. 2014, A&A, 572, A78
Dubrulle, B., Morfill, G., & Sterzik, M. 1995, Icar, 114, 237
Ercolano, B., Jennings, J., Rosotti, G., & Birnstiel, T. 2017, MNRAS, 472, 4117
Flaherty, K. M., Hughes, A. M., Rose, S. C., et al. 2017, ApJ, 843, 150
Flaherty, K. M., Hughes, A. M., Teague, R., et al. 2018, ApJ, 856, 117
Flock, M., Nelson, R. P., Turner, N. J., et al. 2017, ApJ, 850, 131
Fromang, S., & Lesur, G. 2019, in Proc. Astro Fluid, EAS Publication Series 82, ed. A. S. Brun et al., 391
Fromang, S., & Papaloizou, J. 2006, A&A, 452, 751
Goldreich, P., & Lynden-Bell, D. 1965, MNRAS, 130, 125
Gole, D. A., Simon, J. B., Li, R., Youdin, A. N., & Armitage, P. J. 2020, arXiv:2001.10000
Jacquet, E., Balbus, S., & Latter, H. 2011, MNRAS, 415, 3591
Johansen, A., Blum, J., Tanaka, H., et al. 2014, in Protostars and Planets VI, ed. H. Beuther et al. (Tucson, AZ: Univ. Arizona Press), 547
Johansen, A., Klahr, H., & Henning, T. 2011, A&A, 529, A62
Johansen, A., & Youdin, A. 2007, ApJ, 662, 627
Johansen, A., Youdin, A., & Mac Low, M.-M. 2009, ApJL, 704, L75
Klahr, H., & Hubbard, A. 2014, ApJ, 788, 21
Klahr, H., Pfeil, T., & Schreiber, A. 2018, Handbook of Exoplanets (Berlin: Springer), 138
Kowalik, K., Hanasz, M., Wóltański, D., & Gawryszczak, A. 2013, MNRAS, 434, 1460
Krapp, L., Benítez-Llambay, P., Gressel, O., & Pessah, M. E. 2019, ApJL, 878, L30
Laibe, G., & Price, D. J. 2014, MNRAS, 440, 2136
Latter, H. N., & Ogilvie, G. I. 2006, MNRAS, 372, 1829
Lesur, G., Kunz, M. W., & Fromang, S. 2014, A&A, 566, A56
Lin, M.-K. 2019, MNRAS, 485, 5221
Lin, M.-K., & Kratter, K. M. 2016, ApJ, 824, 91
Lin, M.-K., & Youdin, A. N. 2017, ApJ, 849, 129
Lovascio, F., & Paardekooper, S.-J. 2019, MNRAS, 488, 5290
Lyra, W., & Umurhan, O. M. 2019, PASP, 131, 072001
Marcus, P. S., Pei, S., Jiang, C.-H., et al. 2015, ApJ, 808, 87
Morfill, G. E., & Voelk, H. J. 1984, ApJ, 287, 371
Nelson, R. P., Gressel, O., & Umurhan, O. M. 2013, MNRAS, 435, 2610
Nesvorný, D., Li, R., Youdin, A. N., Simon, J. B., & Grundy, W. M. 2019, NatAs, 3, 808
Paardekooper, S. J., & Papaloizou, J. C. B. 2009, MNRAS, 394, 2283
Pinte, C., Dent, W. R. F., Ménard, F., et al. 2016, ApJ, 816, 25
Price, D. J., & Laibe, G. 2015, MNRAS, 451, 813
Pringle, J. E. 1981, ARA&A, 19, 137
Schäfer, U., Yang, C.-C., & Johansen, A. 2017, A&A, 597, A69
Shakura, N. I., & Sunyaev, R. A. 1973, A&A, 24, 337
Shi, J.-M., & Chiang, E. 2013, ApJ, 764, 20
Simon, J. B., Armitage, P. J., Li, R., & Youdin, A. N. 2016, ApJ, 822, 55
Simon, J. B., Armitage, P. J., Youdin, A. N., & Li, R. 2017, ApJL, 847, L12
Simon, J. B., Bai, X.-N., Flaherty, K. M., & Hughes, A. M. 2018, ApJ, 865, 10
Squire, J., & Hopkins, P. F. 2018, MNRAS, 477, 5011
Stoll, M. H. R., & Kley, W. 2016, A&A, 594, A57
Umurhan, O. M., Estrada, P. R., & Cuzzi, J. N. 2019, arXiv:1906.05371
Weidenschilling, S. J. 1977, MNRAS, 180, 57
Whipple, F. L. 1972, From Plasma to Planet in Proc. 21st Nobel Symp., ed. A. Elvius (Wiley: New York), 211
Yang, C.-C., & Johansen, A. 2014, ApJ, 792, 86
Yang, C.-C., Mac Low, M.-M., & Johansen, A. 2018, ApJ, 868, 27
Youdin, A., & Johansen, A. 2007, ApJ, 662, 613
Youdin, A. N. 2011, ApJ, 731, 99
Youdin, A. N., & Goodman, J. 2005, ApJ, 620, 459
Youdin, A. N., & Lithwick, Y. 2007, Icar, 192, 588